2014

Climatology Of The African Easterly Jet And Subtropical Highs Over North Africa And Arabian Peninsula And A Numerical Case Study Of An Intense African Easterly Wave

James D. Spinks
North Carolina Agricultural and Technical State University

Recommended Citation

Spinks, James D., "Climatology Of The African Easterly Jet And Subtropical Highs Over North Africa And Arabian Peninsula And A Numerical Case Study Of An Intense African Easterly Wave" (2014). *Dissertations*. 64.
https://digital.library.ncat.edu/dissertations/64

Climatology of the African Easterly Jet and Subtropical Highs over North Africa and Arabian Peninsula and a Numerical Case Study of an Intense African Easterly Wave

James D. Spinks

North Carolina A&T State University

A dissertation submitted to the graduate faculty

in partial fulfillment of the requirements for the degree of

DOCTOR OF PHILOSOPHY

Department: Energy and Environmental Systems

Major: Atmospheric Science

Major Professor: Dr. Yuh-Lang Lin

Greensboro, North Carolina

2014

The Graduate School
North Carolina Agricultural and Technical State University
This is to certify that the Doctoral Dissertation of

James D. Spinks

has met the dissertation requirements of
North Carolina Agricultural and Technical State University

Greensboro, North Carolina
2014

Approved by:

Dr. Yuh-Lang Lin
Major Professor

Dr. Ademe Mekonnen
Committee Member

Dr. Jin Lee
Committee Member

Dr. Jing Zhang
Committee Member

Dr. Keith Schimmel
Department Chair

Dr. Li-Ping Liu
Committee Member

Dr. Sanjiv Sarin
Dean, The Graduate School

Biographical Sketch

James D. Spinks was born on May 25, 1984, in Greensboro, North Carolina. He attended Asheboro High School in Randolph County. He received his Bachelor of Science degree in Applied Mathematics on August 2006 at Winston-Salem State University. He entered into the Master of Science program in Applied Mathematics in the Department of Mathematics at North Carolina Agricultural and Technical State University in August 2007 and began his thesis research with Dr. Guoqing Tang and Dr. Yuh-Lang Lin in 2008 and received his Masters in December 2009. In Fall 2010, he started his Ph.D research under Dr. Yuh-Lang Lin.

Dedication

This dissertation is dedicated to those that have supported me throughout my endeavors of earning a Ph.D. Thanks to my loving wife and daughter, LaTonya and Jayel Spinks, for their continuous support and uplifting spirits. Without them, this dissertation would not have been possible. Thanks to my mother and father, James and Betty Spinks, for their encouragement and raising me well. I would also like to thank my big brothers Taraus Spinks and Wilson Jones for keeping me on track during life, as well as, my big sister Gail Brunson for introducing me to higher level education.

I would also like to dedicate this dissertation to those who have passed away during my path to a Ph.D.: Jackie Ray Cheek, Margret Cheek, Sam Spinks, Jake Spinks, Josephine Spinks, Russell Murphy, and Christine Fennell. They were my source of inspiration and motivation growing up.

Finally, I would like to dedicate this dissertation to family and friends who have stuck by me and believed in me: Rosa Mae Marsh, Homer Marsh, Beverly Mitchell, LaRhonda Mitchell, Tiaja Spinks, Tiante, Spinks, Donavon Horton, Pat Marsh and family, Lynn Marsh, Beverly Ferris and family, the Goins family, Uncle D, Annie Rouse, Michael Rouse, Felicia Rouse, Charles and Bob Alston, June McLean and family, Gerrick Williams, Gwendolyn Williams, Cory Nicolson and family, Alton Mills and family, RaShad McGee and family, Edna Johnson and family, and A. J. Wone.

Acknowledgments

First, I would like to thank my thesis advisor, Dr. Yuh-Lang for his continuous support and belief in me and for his mentorship. Without his advisement and supervision, this thesis would not be possible. I would also like to thank my thesis committee members, Dr. Jin Lee of NOAA ESRL, Dr. Ademe Mekonnen and Dr. Jing Zhang of EES, and Dr. Li-Ping Liu of the Department of Mathematics at North Carolina Agricultural and Technical State University for agreeing to serve on my dissertation committee, and for their encouragement, help and support. The EES Department chair Dr. Keith Schimmel, Dr. Solomon Bililign, Mathematics department chair Dr. Guoqing Tang, and the NCAT modeling group have been my resources of support and helped me grow both professionally and personally. *This work is supported by NOAA Educational Partnership Program under the cooperative agreement A06OAR4810187.*

Table of Contents

List of Figures

List of Tables

List of Abbreviations

A04	August 2004
AEJ	African Easterly Jet
AEW	African Easterly Wave
ARW	Advanced Research Weather and Research Forecast (WRF) model
CFSR	Climate Forecast System Reanalysis
CPC FEWS	Climate Prediction Center's Famine Early Warning System
ECMWF	European Centre for Medium-Range Weather Forecasts
ENSO	El Nino-Southern Oscillation
ERA-40	European Centre Medium-Range Weather Forecast 40-Year Reanalysis
ERA-I	European Centre Medium-Range Weather Forecast Reanalysis Interim
ESRL	Earth Systems Research Laboratory
ITCZ	Intertropical Convergence Zone
ITF	Intertropical Front
LWM	Local Wind Maximum
LWM_E	Local Wind Maximum East
LWM_W	Local Wind Maximum West
MCS	Mesoscale Convective System
MEI	Multivariate ENSO Index
NCDC	National Climate Data Center
NCEP	National Centers for Environmental Prediction
NOAA	National Oceanic and Atmospheric Association
PAM	Pre-African Easterly Wave and Mesoscale Convective System

TEJ	Tropical Easterly Jet
WRF	Weather Research and Forecasting model

Abstract

North African climate is analyzed between 1979 and 2010 with an emphasis on August using the European Center for Medium Range Weather Forecast (ECMWF) global dataset to investigate the effects of the subtropical anticyclones over North Africa and the Arabian Peninsula on the Africa easterly jet (AEJ). It was found that the AEJ encloses a core with a local wind maximum (LWM) in both West and East Africa, in which the west LWM core has a higher zonal wind speed. The strength of both cores is distinctly different by way of thermal wind balance.

The variability of these synoptic weather features is higher in East Africa. The most noticeable variability of intensity occurred with easterly waves. Maintenance of easterly waves from the Arabian Peninsula into East Africa is dependent on strong zonal gradients from the AEJ. These zonal gradients were induced by the strengthening of the subtropical highs and the presence of a westerly jet in Central Africa and south of the Arabian Peninsula. During positive ENSO periods, these systems are generally weaker while in negative periods are stronger.

The origins of an intense African easterly wave (AEW) and mesoscale convective system (MCS) in August 2004 (A04) were traced back to the southern Arabian Peninsula, Asir Mountains, and Ethiopian Highlands using gridded satellite (GridSat) data, ERA-I, and the WRF-ARW model. A vorticity budget was developed to investigate the dynamics and mechanisms that contribute to the formation of A04’s vorticity perturbation.

CHAPTER 1

Introduction

Weather and climate over North Africa have been studied extensively to understand the impacts of synoptic systems, such as subtropical highs or anticyclones, African easterly waves, and their climate variability, on the environment, such as African easterly jets and tropical cyclones. In this dissertation, we will investigate (a) effects of the subtropical anticyclones on the African easterly jet, (b) variability of the of the subtropical highs, African easterly jet and easterly wave intensities, and (c) formation of African easterly waves and mesoscale convective system by making climate and synoptic data analyses and numerical simulations using a numerical model.

1.1 Effects of the Subtropical Anticyclones on the African Easterly Jet

The African easterly jet (AEJ) is a synoptic feature over North Africa, which is a localized wind maximum embedded in an easterly wind flow in the mid-troposphere at 600 mb. Several questions regarding the roles played by the AEJ contributing to North African climate and weather have been raised in the past. A number of studies have been devoted to achieving a better understanding of the formation and maintenance of the AEJ, but most of the research has been done in West Africa. For example, Cook (1999) examined the dynamics of the AEJ while Thorncroft and Blackburn (1999) and Chen (2005) investigated the maintenance of the AEJ. Very few studies of AEJ are focused on East Africa, which is the focus of this study.

Dezfuli and Nicholson (2010) investigated the structure of the AEJ over a 56-year period and examined a second wind maximum of the AEJ located in East Africa around 20°E, whose amplitude varies per year for the month of August. A careful inspection of the 56-year long mean of the AEJ in Fig. 1 from Dezfuli and Nicholson (2010) reveals that a second maximum exists further east of 30°E; however, the authors noted that a second maximum does not exist from the long term mean of the AEJ. In contrast, Cook (1999) did a comparison of the European Centre Medium-Range Weather Forecast 40-Year Reanalysis (ERA-40) (Uppala et al. 2005) and National Center of Environmental Prediction (NCEP) reanalysis (Kalnay et al. 1996) data analyzing the AEJ and there was a second wind maximum located around 40°E in the ERA-40 data, but the author did not address the second wind maximum.

The AEJ is located between dry Saharan (20°N – 35°N) and moist tropical (5°N – 20°N) regions. The AEJ lies between 600 and 700 mb and exists as a result of the positive meridional temperature gradient (Cook 1999, Thorncroft and Blackburn 1999, Parker et al. 2005, Cornforth et al. 2009). Grist et al. (2002) observed the mean speed of the LWM_W for the month of August to be 10 to 12 m s^{-1}. Another observation was from the Jet2000 project (Thorncroft et al., 2003) that examined the LWM_W to have a much stronger zonal speed of 21 m s^{-1}, which was higher than the climatological average value of 15 m s^{-1} (e.g., Reed et al., 1977). Dezfuli and Nicholson (2010) observed the LWM_W to have a mean speed of 13.5 m s^{-1} and the LWM_E to have a mean speed of 12.7 m s^{-1}.

The North African climate during summer includes synoptic features that influence the AEJ patterns on the continent, which consist of the Tropical Easterly Jet (TEJ) in the upper troposphere, the Saharan high in the mid-troposphere, Saharan thermal low in the lower troposphere, and the Inter Tropical Convergence Zone (ITCZ) (Wu et al. 2009). There is also a low-level convergence zone located at 20°N in North Africa, which is also known as the Intertropical Front (ITF). The maximum vertical motion associated with the ITF is tilted toward the south with height into the mid-troposphere between 10°N and 15°N, which is collocated with the ascending branch of the Hadley Cell. The location of the Hadley Cell ascending branch is where the highest rainfall occurs and is often referred to as the ITCZ.

Warm temperatures dominate the continent causing a rather unstable atmosphere. The cooler temperatures in the tropical region are a result of temperature advection from the Gulf of Guinea due to the African monsoon westerlies. Northward flow onto the continent across the Guinean coast curves eastward to form the equatorward section of cyclonic flow about a thermal low centered over Saharan Africa (Cook 1999, Lavaysse 2009). The Saharan thermal low effects the troposphere from the surface up to about 600 mb and can be found along the ITF where buoyancy produces vertical motion forcing warm air into the mid-atmosphere and causing convergence at lower levels (Wu et al., 2009). The low-level convergence and upper-level divergence over the continent constitute a secondary circulation that concentrates cyclonic vorticity at the lower levels and anticyclonic vorticity at the upper levels (Holton 2004, Lavaysse 2010).

Chen (2005) described the role that the Saharan high plays on the LWM_W intensity by observing the circulation patterns over Africa. The lower-tropospheric monsoon southerly flow over West Africa is established by the lower branch of the Hadley circulation. The TEJ in the upper troposphere is located aloft over the upward branch of the Hadley circulation, while the LWM_W is placed over the downward branch of the Saharan circulation**.** The upward (hot) vertical motion driven by the thermal low heating and the downward (cold) branch of the Indian monsoon form a strong divergence center. The link between the upper and lower tropospheric circulation over North Africa can be established through this divergence center. The Saharan high covers most of North Africa between 20°W and 20°E.

1.2 Variability of the Subtropical Highs, African Easterly Jet and Easterly Wave Intensities

Over North Africa and Arabian Peninsula, there exist several synoptic systems that influence weather patterns in late summer significantly, such as Saharan and Arabian highs, the African easterly jet (AEJ), and easterly waves over Arabia and African easterly waves (AEWs) in mid-troposphere, such as 600 mb. In particular, during the month of August, North Africa has been observed to be very active with easterly waves along with an unstable mid-tropospheric jet. In addition, North Africa experiences its most active month for precipitation in August.

Spinks et al. (2014) investigated the AEJ and local wind maxima in West (LWM_W) and East (LWM_E) Africa, respectively, to the Saharan and Arabian highs. In their study, an analysis of the European Centre for Medium-Range Weather Forecasts Intermediate Reanalysis (ERA-Interim) at 0.75° for the month of August over 32 years (1979-2010) was carried out to compare the differences of the AEJ's maintenance and formation associated with LWM_W and LWM_E. In this research, we plan to extend the study of Spinks et al. (2014) to investigate the yearly variability of AEJ, LWMs, easterly waves and AEWs in their intensities over North Africa and the Arabian Peninsula during the same period. The sensitivities of these features to El Nino-Southern Oscillation (ENSO) will be studied. Points of interest include displacements of the LWMs and anticyclonic systems, structure of the AEJ, and relative vorticity intensities.

The subtropical high pressure system over North Africa and the Arabian Peninsula has been investigated in previous studies to show its relationship with the AEJ. Chen (2005) described the formation and maintenance of the Saharan high through divergent fields of velocity potential. It was shown that the divergent center was formed from east-west differential heating by thermal low heating (hot) and downward (cold) branch of the Indian Monsoon. Similar procedure was performed by Spink et al. (2014) for the Arabian high. With the usage of a higher spatial resolution data set, two divergent centers were illustrated respectively for the Saharan and Arabian highs. In particular, the divergent center over Arabia was more intense due to the higher temperatures and colder sinking air from the upper troposphere.

It is well known that the AEJ is formed through baroclinicity (Cook 1999, Thorncroft and Blackburn 1999, Cornforth et al. 2009, Wu 2009), but the existence of the LWMs within the AEJ are from the meridionally induced pressure gradient from the anticyclonic centers of the Saharan high and Arabian high. The Arabian high serves as a maintenance mechanism for the LWM_E, which in turn, aids easterly waves propagating from a genesis area located between 45°E and 55°E along the southern coast of the Arabian Peninsula into East Africa (Lin et al. 2013). This genesis area of vorticity is induced by the convergence of northerly winds and southerly winds from the Indian Ocean highs (Rao 2003).

The ENSO (Bjerknes 1969, Philander 1990) index will also be used in this research. In order to further understand the variability of the AEJ to African climate; it is necessary to investigate how ENSO affects changes in Africa. Hulme et al. (2001) noted that ENSO is a possible key driver on potential African climate variability. Kruger and Shongwe (2004) examined whether ENSO had any effects on the inclination in temperature, in particular for the late austral summer period. They concluded that increases in late summer temperatures are not forced by the occurrence of ENSO and Non-ENSO events (Collins 2011). Semazzi and Indeje el al. (1999) presented how ENSO affects the rainfall variability in East Africa, in which they concluded that ENSO plays a significant role in determining the monthly seasonal rainfall patterns in the East African region. Collins (2011) investigated the temperature variability over Africa with comparisons to the ENSO index and concluded that in June, July, and August one can observe warming throughout the whole continent. Chen (2005) suggested the North African climate systems may well be established through the effects of ENSO on the Asian monsoon's east-west circulation and in turn on the Saharan high.

1.3 Formation of an African Easterly Wave and Mesoscale Convective System

An easterly wave is a migratory wavelike disturbance of the tropical easterlies within a broad easterly current and moves from east to west, generally more slowly than the current in which it is embedded (Glickman 2000). Best described in terms of its wavelike characteristics in the wind field, it also consists of a weak trough of low pressure. To the west of the trough line in an easterly wave over the ocean, there is generally found divergence, a shallow moist layer, and exceptionally fine weather. The moist layer rises rapidly near the trough line; in and to the east of the trough line intense convergence, much cloudiness, and heavy rain showers prevail. This asymmetric weather pattern may be greatly distorted by orographic and diurnal influences if the wave passes over land areas. Thus, African easterly waves (AEW) may be defined as easterly waves observed over North Africa. Observational analyses indicated that AEWs possess the following basic characteristics (Reed et al., 1977; Burpee, 1974; Chen, 2006): (1) a propagation speed of 7 – 9 ms^{-1}, (2) a wavelength of ~2000 – 4000 km, and (3) propagating along the rainy zone and to the south of the African easterly jet (AEJ) around 10^{o}N (AEW$_{s}$) or along the Saharan thermal low near 20^{o}N (AEW$_{n}$).

Several mechanisms have been proposed for the formation of AEWs in previous studies: (1) Charney-Stern (1962) barotropic-baroclinic instability (Burpee 1972, Chen 2006), which is more relevant to AEW$_{s}$s (South) (Rennick 1976; Mass 1979; Kwon 1989; Thorncroft and Hoskins 1994a; (2) baroclinic instability (Chang 1993; Thorncroft 1995) which is more relevant to AEW$_{n}$s (North). Also included is the proclaimed African Easterly Jet (AEJ) instability (e.g., Simmons 1977; Thorncroft and Hoskins 1994a, b; Grist et al., 2002), which is assisted by the baroclinicity associated with the Sahara Desert; (3) latent heating (e.g., Hsieh & Cook 2005, 2007; Thorncroft et al., 2008); and (4) orographic forcing (Mozer & Zehnder 1996; Lin et al., 2005). In later work for pre-Debby (2006) AEW-MCS (Lin et. al 2013), it was found that an interaction between northerly Shamal wind and southerly wind from the India Ocean anticyclone could generate cyclonic vorticity over the southern Arabian Peninsula.

AEWs are often associated with mesoscale convective systems (MCS) while they travel westward across the African continent (e.g., Payne & McGarry, 1977; Laing & Fritsch, 1993; Fink & Reiner, 2003). This helps alter convection and rainfall over the African continent on a daily basis (e.g., Carlson, 1969) and makes AEWs detectable from satellite imagery. MCSs tend to occur in preferred regions of AEWs: at or ahead of the AEW trough in the vicinity of the intertropical convergence zone (ITCZ), and collocated with the trough over the ocean. Hill and Lin (2003) and Lin et al. 2005, back-tracked the pre-Alberto AEW-MCS (2000) precursor to the Ethiopian Highlands, while Berry and Thorncroft (2005, 2008) and Mekonnen et al. (2006) found that the Darfur Mountains are particularly important for providing convective precursors that propagate westward and trigger AEWs downstream.

Hodges and Thorncroft (1997) statistically showed that northern Africa could be divided into areas of genesis or lysis regions for growing or dissipating convection, respectively. They tracked several MCSs across northern Africa using the coldest cloud-top temperatures and then the areas were averaged into the appropriate convective regions for genesis or lysis. Other studies have also shown that most MCSs formed in baroclinic zones and downstream of mountain ranges (Laing & Fritsch, 1993), such as the case over northern Africa during the Northern Hemisphere summer months.

An easterly wave was traced back to a vorticity genesis region identified by Lin et al. (2013). This region is located over the southern Arabian Peninsula and was investigated to see formation and evolution of the pre-Debby AEW-MCS. For this study, we will concentrate on the origin of a coupled *AEW-MCS in August of 2004* (denoted as A04, hereafter) while taking a similar approach that was used to explain vorticity generation in Lin et al. (2013). The pre-MCS/convective clusters and pre-AEW/vorticity perturbation associated with A04 will be examined to understand the mechanisms that generate these systems. It has been observed that mountains in East Africa and the Arabian Peninsula may generate vorticity and MCSs, especially during diurnal cycles (Hill and Lin 2003). This study focus will on the wind and vorticity fields along with convection to identify A04’s origins and the mechanisms that generate vorticity perturbations.

CHAPTER 2

Effects of the Subtropical Anticyclones over North Africa and Arabian Peninsula on the African Easterly Jet

2.1 Statement of Problem

In this study we will address the AEJ and its two wind maximums over East Africa, West North Africa and the Arabian Peninsula for 32 years of August between 1979 and 2010 with case study of 2006. We will also explore the dynamics of the Saharan and Arabian highs, and why the East Local Wind Maximum (denoted as LWM_E hereafter) is weaker than the West LWM (denoted as LWM_W hereafter). August was chosen because it is the peak rainfall month over East Africa.

2.2 Data and Methodology

Over the years, climatological analyses of the AEJ were carried out using global model data with relatively low spatial resolutions. Cook (1999) investigated the AEJ and its formation using the NCEP reanalysis data for the month of July between 1957 and 1996. This dataset consists of a resolution of 2.5° x 2.5° globally. Chen (2005) used the NCEP reanalysis data for June, July, and August between 1979 and 2002 to study the AEJ in relation to the Saharan high. Chen (2006) also used the ERA-40 dataset with a 2.5° x 2.5° global grid for the summer months of June, July, August, and September between 1991 and 2000 to examine African easterly waves (AEWs), the AEJ, and Saharan high. Dezfuli and Nicholson (2010) analyzed the AEJ using the NCEP reanalysis dataset for the month of August between 1948 and 2003 on a monthly time scale.

In this study, we will use the ECMWF-Interim (ERA-I) reanalysis data with a spatial resolution of 0.75° x 0.75° global for the month of August between 1979 and 2010 (Dee et al.

2011). The investigation of the AEJ structure and intensity from previous studies that used the NCEP reanalysis or the ERA-40 may vary from this research. Limitations of the NCEP data and ERA-40 would include their lower spatial resolution and the discrepancies of the AEJ intensity.

Figure 2.1 illustrates the LWM_E at 600 mb from various datasets to confirm consistency in this feature. The ERA-I and Climate Forecasting System Reanalysis version 1 (CFSR) at 0.3° (Saha et al. 2006) show a clear depiction of the LWM_E in East Africa (Figure 2.1a and c) for the month of August between 1979 and 2010. There is an indication of a very small and weak LWM_E in the ERA-40 (Figure 2.1b) and NCEP reanalysis (Figure 2.1d) datasets. The little resolve of the LWM_E from these respected datasets is due to the size of the $LWM_{E.}$ Based on the ERA-I and CFSR, the LWM_E is about 10° (~1100 km) in length and 3° in width. With the spatial resolution of the ERA-40 and NCEP reanalysis being 2.5°, this would leave about 4 grid points for the ERA-40 and NCEP reanalysis to resolve the LWM_E. The LWM_E is prominent in all of the presented datasets at 550 and 500 mb (not shown).

2.3 Results

2.3.1 Synoptic Features and Circulation over North Africa. To explore the circulation of subtropical anticyclones, we use streamfunction as a diagnostic variable. For the month of August between 1979 and 2010, the major atmospheric features are depicted in Figure 2.2. As seen in Figure 2.2a, the TEJ axis is located on the southern rim of the Tibetan high with the TEJ intensity decreasing from east to west. The maximum intensity of the TEJ is located to the south of the Tibetan anticyclone center and extends into the southwestern Arabian Peninsula and East Africa.

At 600 mb (Figure 2.2b), two high pressure systems are shown: the Saharan high around (10°W, 25°N) and the other is the Arabian high around (40°E, 25°N). The AEJ axis is located to the south of the anticyclonic circulations around (17°W-45°E, 10°N-20°N). The intensity of the LWM_E at (35°E, 15°N) has a zonal wind speed average of -9.81 m s^{-1} and the intensity of the

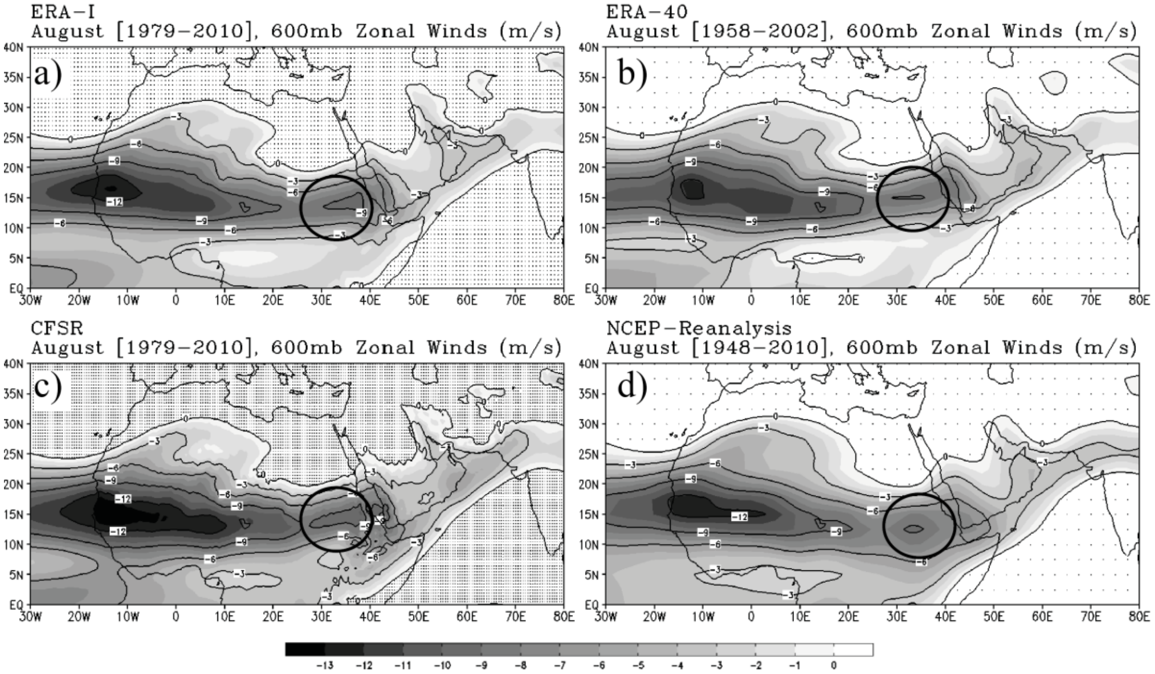

Figure 2.1. The 600 mb zonal wind is depicted to show the local wind maximum east (black circle) in different datasets. The shade is for easterly winds every 1 m s^{-1}, the contours are easterly winds every 3 m s^{-1}, and the stippling indicates grid spacing of respected dataset for westerly winds, (a) the European Centre Medium-Range Weather Forecast Intermediate reanalysis on a 0.75° grid with zonal averages for the month of August between 1979 and 2010, (b) the European Centre Medium-Range Weather Forecast 40-Year reanalysis on a 2.5° grid with zonal averages for the month August between 1958 and 2002, (c) the Climate Forecasting System (version 1) reanalysis on a 0.3° grid with zonal averages for the month of August between 1948 and 2010, and (d) the National Center of Environmental Prediction reanalysis on a 2.5° grid with zonal averages for the month of August between 1979 and 2010.

LWM_W at (17°W, 18°N) has a zonal wind speed average of -13.41 m s^{-1}. Note that the LWM_W and Saharan high are much stronger than the corresponding LWM_E and Arabian high.

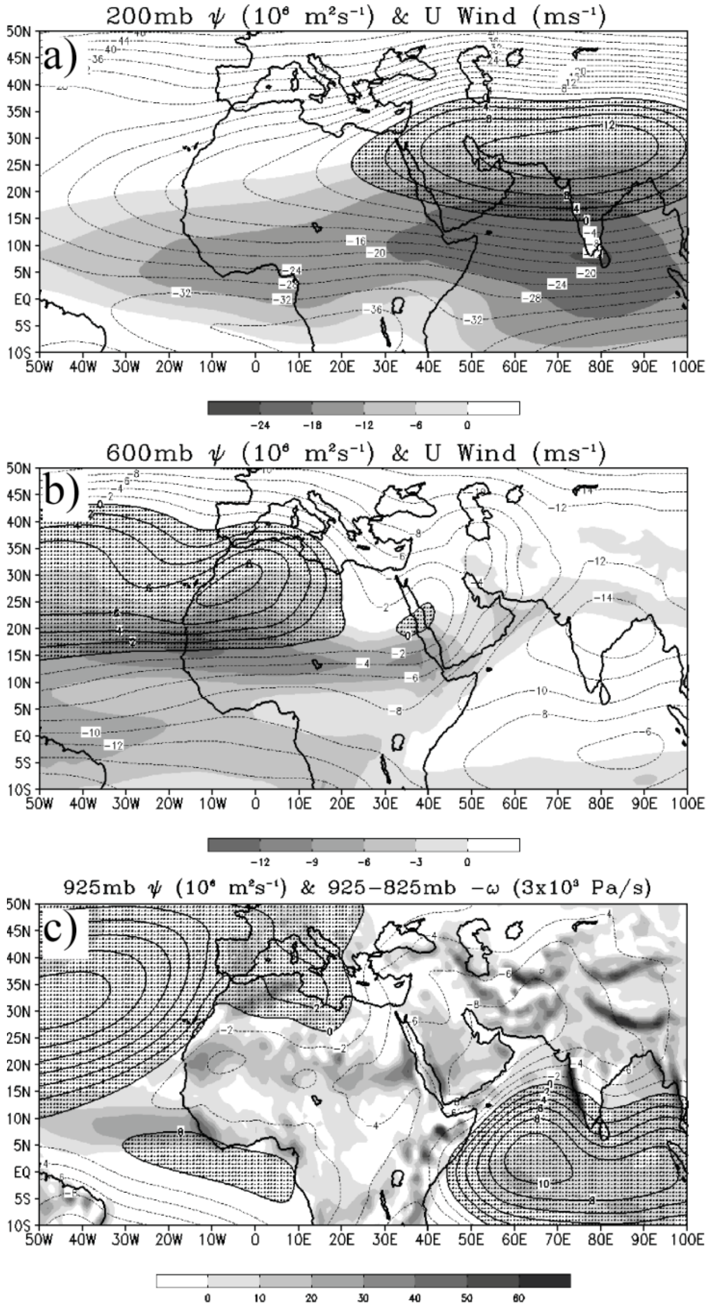

Figure 2.2. August 32-year (1979 – 2010) average of (a) 200 mb streamfunction (ψ) (x 10^6 m^2 s^{-1}) contoured every 2 m^2 s^{-1} and zonal velocity shaded every 6 m s^{-1}, (b) 600 mb streamfunction contoured every 2 m^2 s^{-1} and zonal velocity shaded every 3 m s^{-1}, and, (c) 925 mb streamfunction contoured every 2 m^2 s^{-1} and averaged 925-825 mb vertical velocity (3x10^3 Pa s^{-1}) shaded every 10 Pa s^{-1}.

At 925 mb, two major anticyclonic systems are located over the Atlantic and Indian Oceans. In Figure 2.2c, the ITF can be depicted using upward motion ($-\omega<0$) where there is strong baroclinicity along the convergence zone. Across North Africa at 20°N, the converging winds from the Guinea Monsoon and the northerly Harmattan flow are effects from the generation of the Saharan thermal low (15°W, 20°N). Several intense upward motion regions exist across North Africa as part of the ITF heating. There is a strong vertical motion on the lee side of the Darfur Mountains around (20°E, 20°N), on the lee side of the northern most part of the Ethiopian Highlands around (35°E, 20°N), and another over the Asir Mountains around (43°E, 20°N). The intense vertical motion over the Arabian Peninsula is associated with the Arabian thermal low.

Exploring the east-west circulation will provide insight on how the anticyclonic systems are maintained. The streamlines on a zonal and meridional vertical cross section of North Africa depicts the east-west circulation (Figure 2.3a) along the ITF approximately 20°N, the north-south Hadley Circulation over West Africa (10°W-15°W) (Figure 2.3b), and the north-south Hadley Circulation over East Africa (35°E -40°E) (Figure 2.3c). The east-west circulation was computed using the magnitude of zonal winds (u) and negative omega ($-\omega$). Figure 2.3a illustrates the intense upward motion caused by the Saharan thermal heating and Arabian thermal heating along the ITF. Warm air is lifted into the mid-troposphere, in which it will converge with the sinking cooler air from the upper-troposphere. The strong divergence from the vertical flow can be seen at the mid-troposphere located between 600 and 400 mb in West Africa and 600 to 500 mb in East Africa. This indicates that the Arabian high is shallower in comparison to the Saharan high. Similar divergent flows can be found on meridional cross sections averaged between 10°W to 15°W (Figure 2.3b) and 35°E to 40°E (Figure 2.3c). Figure 3b is a vertical cross section over the Saharan thermal low and Figure 2.3c is a vertical cross section over the Arabian thermal low.

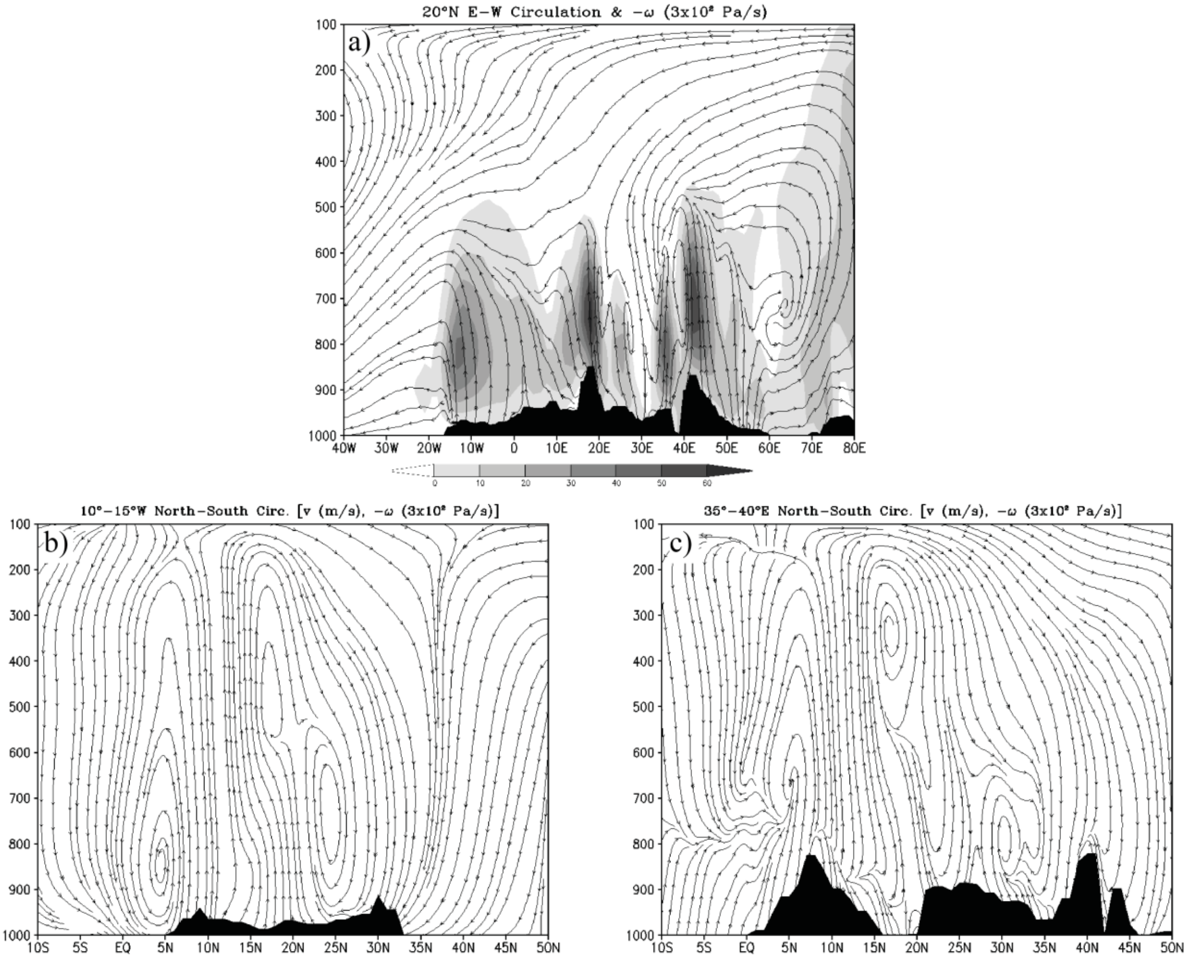

Figure 2.3. August 32-year (1979 – 2010) average of (a) zonal vertical cross section at 20°N of *u* and -*ω* (3 x 10^2 Pa s^{-1}), (b) meridional vertical cross section of *v* (m s^{-1}) and -*ω* (3 x 10^2 Pa s^{-1}) along 10°W – 15°W and (c) meridional vertical cross section along 35°E – 40°E of *v* (m s^{-1}) and -*ω* (3 x 10^2 Pa s^{-1}).

Figure 2.3b and c are the magnitude of meridional winds (*v*) and negative omega (-*ω*). The ITCZ is located between the southern Hadley Cell (south of 10°N) and the northern Hadley Cell (north of 10°N) with divergent flow in the upper troposphere. This is consistent with

Chen’s (2005) findings on the divergent flow from the northern and southern Hadley Cell interaction. The cross section in Figure 2.3c reveals similarities of a divergent flow present in the upper-troposphere. There exists a Hadley Cell to the north and south of the ITCZ in the eastern African region. The ITF in East Africa starts in the lower troposphere around 20°N, and then tilts to the south around 12°N in the mid-troposphere where the strongest vertical motions are located.

To get a better understanding of the flow field across North Africa at 600 mb, the streamfunction (Figure 2.2b) and velocity potential fields (Figure 2.4) have been compared. The streamfunction field shows the rotational flow of the Saharan and Arabian highs. Between these two anticyclones is a trough located around (25°N, 30°E). On the east side of the Saharan and Arabian highs are strong northerly flows that advect hot and dry air into latitudes lower than 20°N. The velocity potential maxima are located to the southeast of the Sahara Desert center and south of the Arabian high center (Figure 2.4). These divergent centers are formed and maintained from the east-west differential heating induced by the upward branch of the Saharan thermal low and Arabian thermal low heating and cooling from the downward branch of the TEJ, as shown in Figure 2.3a from the east-west circulation. This east-west differential heating serves as a maintenance mechanism for the Saharan and Arabian highs.

The divergent center over the Arabian Peninsula is more intense than the divergent center over central Africa since the temperatures over the Arabian Peninsula are hotter than the Saharan Desert (Figure 2.5). The Arabian thermal heating influences the northerly “Shamal” wind (e.g., Rao 2003, Lin et al. 2013) and is affected by the southwesterly Somali jet (Hurlburt and Thompson 1979) from northern Indian Ocean. These winds converge on the east side of the Asir Mountains in the vicinity of the ITCZ. The vertical motion from the Arabian thermal heating is just as intense as the vertical motion associated with the Saharan thermal heating, but with the exception of higher temperatures over the Arabian Peninsula.

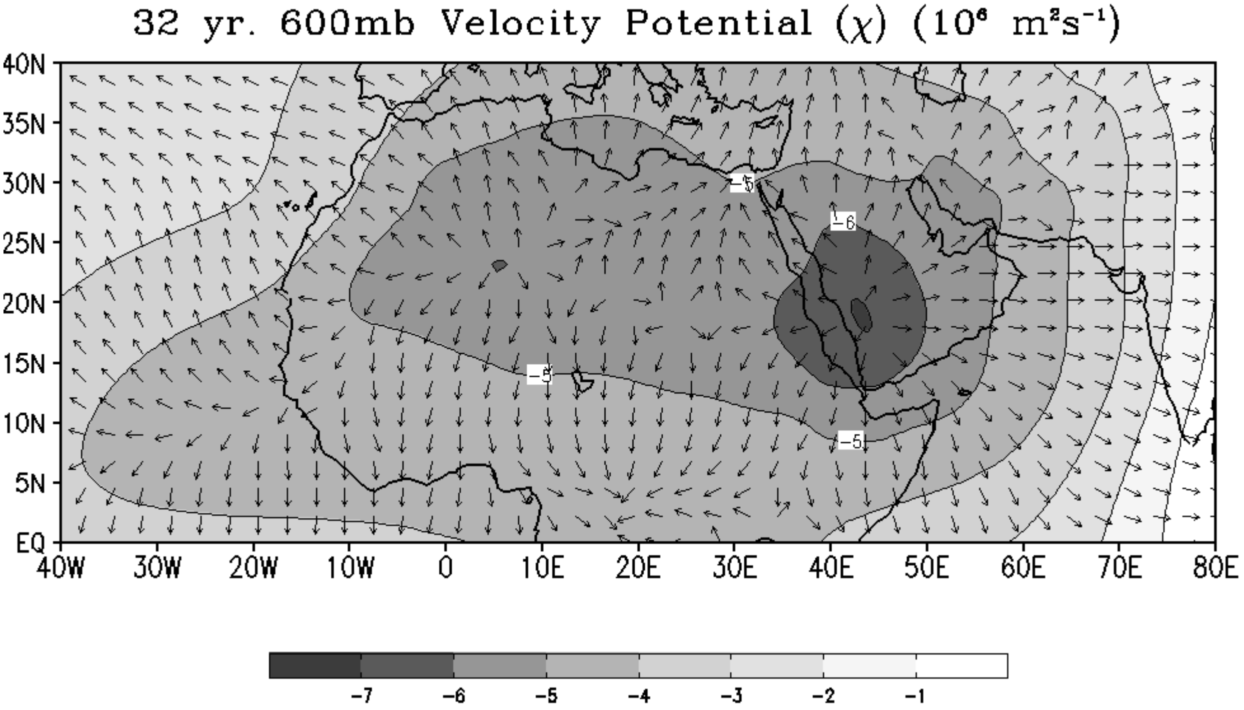

Figure 2.4. August 32-year (1979 – 2010) average of 600 mb velocity potential (χ) (10^6 m^2 s^{-1}) shaded and contoured every -1 m^2 s^{-1} starting at 0 with irrotational wind vectors to show divergence.

2.3.2 Characteristics and Formation of the LWM_E and LWM_W. Figure 2.6a depicts the potential vorticity field over North Africa. The intensity of the potential vorticity field increases from east to west starting around 40°E. This is directly correlated with the growth of the AEJ and AEWs from the potential vorticity gradient. In Figure 2.6b, the reversal of the meridional potential temperature gradient can be seen between 600 mb and 500 mb levels for both LWMs. The AEJ is a response to the surface baroclinicity and reversal of the temperature gradient that displaces the AEJ in the mid-troposphere (Burpee 1972, Cook 1999, Thorncroft and Blackburn 1999). The negative potential vorticity gradient is also the strongest between 600 and 500 mb.

The dynamics of this have been well-observed in previous literatures for the $\mathrm{LWM}_{\mathrm{W}}$. Similar dynamical processes hold true for the $\mathrm{LWM}_{\mathrm{E}}$ except that the $\mathrm{LWM}_{\mathrm{E}}$ is displaced at slightly higher levels around 550 mb, but is still present at 600 mb. This includes the Darfur Mountains between 20°E and 25°E, the northern portion of the Ethiopian Highlands between 35°E and 40°E, and the Asir Mountains between 43°E and 50°E. The TEJ in the upper atmosphere around 100 mb also exhibits the same dynamics as the AEJ with the negative meridional potential vorticity gradient and reversal of the meridional potential temperature gradient.

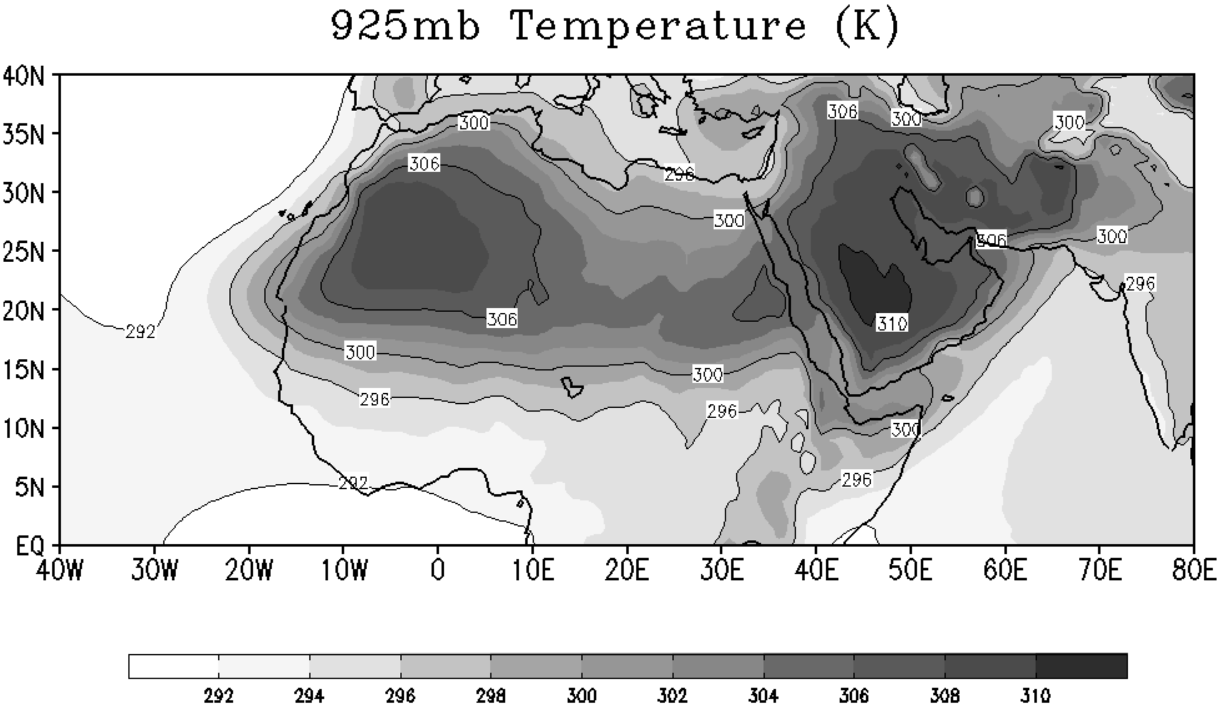

Figure 2.5. August 32-year (1979 – 2010) average of 925 mb temperature (K) shaded every 2 K and contoured ever 4 K.

In the literature, the anticyclonic systems have been presented using streamfunction to show circulation. Simply taking the negative meridional gradient of streamfunction (not shown) will result in zonal wind with near real zonal wind estimations for the AEJ. In this study, we want to show how close the zonal geostrophic winds are to real zonal wind using the thermal wind relationship since understanding of it will help distinguish the differences of the LWM_E and the LWM_W.

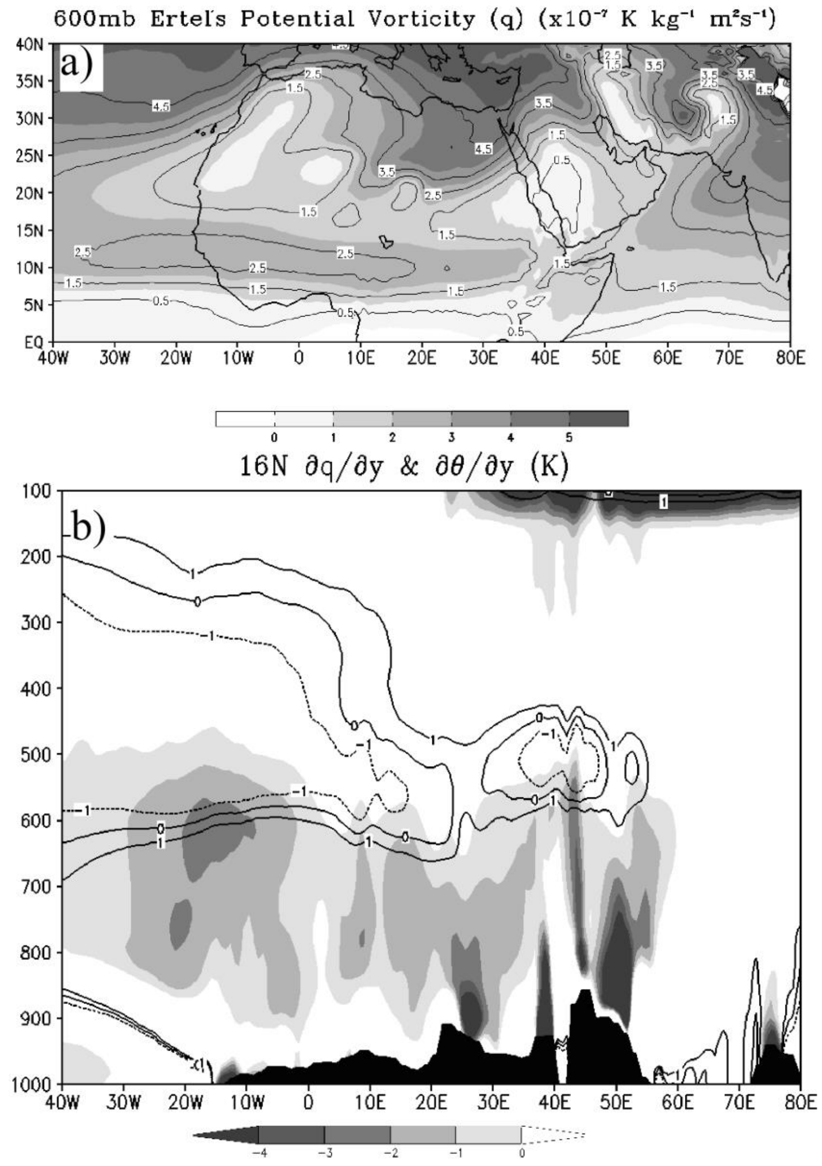

Figure 2.6. August 32-year (1979 – 2010) average of average of (a) 600 mb Ertel's potential vorticity ($x10^{-7}$ K kg^{-1} m^2 s^{-1}) field shaded every 1 K kg^{-1} m^2 s^{-1} from 1 K kg^{-1} m^2 s^{-1} to 5 K kg^{-1} m^2 s^{-1} and contoured every 1 K kg^{-1} m^2 s^{-1} from 0.5 K kg^{-1} m^2 s^{-1} to 5.5 K kg^{-1} m^2 s^{-1}, (b) is the vertical cross section at 16°N of the meridional potential vorticty gradient (shaded), and meridional potential temperature gradient (K) (contours) with a contour interval of [-1, 0, 1].

The baroclinicity is strong in West Africa, East Africa and the Arabian Peninsula (Figure 2.7a), but the LWM_E is weaker and smaller than the LWM_W. This raises the question we want to address: Why is the LWM_E weaker than the LWM_W? We hypothesize that the intensity of the weak LWM_E is caused by a weak mid-tropospheric high. Figure 2.7b illustrates the connection with the geostrophic wind maxima, which are associated with the Saharan high and Arabian high induced meridional geopotential gradients, respectively. The LWMs are located around 600 and 550 mb directly over the zonal geostrophic maxima in West Africa and East Africa. Since the Saharan high is more intense and broader than the Arabian high, the Saharan high produces a much stronger meridional geopotential gradient in West Africa, thus the making the LWM_W stronger than the LWM_E. The AEJ will be formed at 600 mb with an elongated easterly zonal geostrophic flow generated from baroclinicity. The presence of the Saharan and Arabian highs will increase easterly flow to the south of the anticyclonic centers because of the increased meridional geopotential gradient. This geopotential gradient along with the dominant influence from baroclinicity helps give the AEJ two distinct zonal maxima in East and West North Africa.

The local easterly zonal wind extends into the Arabian Peninsula along with a strong meridional temperature gradient, but a weakened meridional geopotential gradient. There is no LWM present over the Arabian Peninsula region. The AEJ decreases in intensity as a result of the meridional geopotential gradient decreasing, but the meridional temperature gradient remains intense across the southern Arabian Peninsula primarily because of the land-sea temperature contrast.

2.3.3 Case Study for 2006: Evolution of the Anticyclones and LWMs. In the following, we will be looking at the LWM’s dynamics over a 32-year period for August to a smaller time scale for 2006 while highlighting August for a 6 hourly time scale analysis. It is important to observe evolution of synoptic features to examine when the LWM_E is formed.

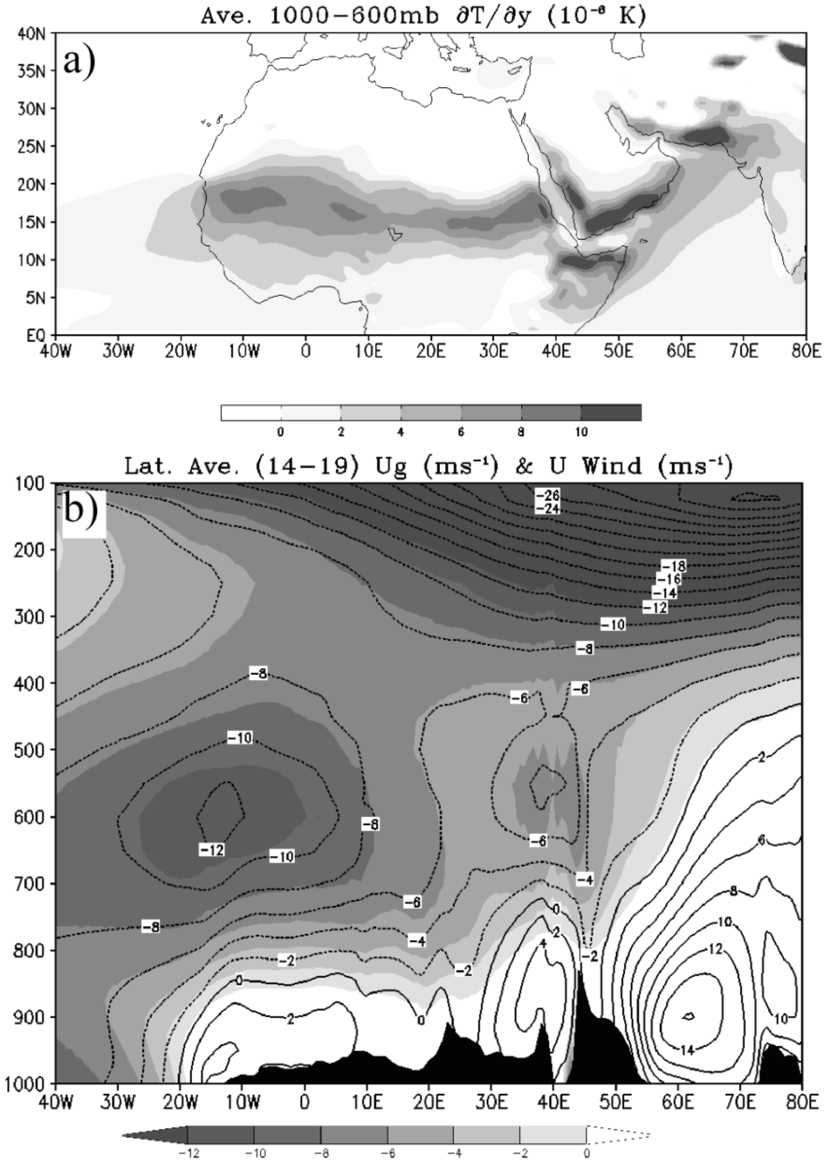

Figure 2.7. August 32-year (1979 – 2010) average of (a) the meridional temperature gradient (10^{-4} K) averaged between 1000 to 600 mb shaded every 2 K starting at 0 and meridional geopotential gradient contoured every 1 gmp starting at 0 and (b) vertical cross section between 14°N and 19°N of geostrophic wind (m s^{-1}) shaded every -2 m s^{-1} starting at 0 and zonal wind (m s^{-1}) contoured every 2 m s^{-1}. The terrain is crossed at 16°N.

Figure 2.8 emphasizes the correlation of the Saharan high/LWM_W and Arabian high/LWM_E using daily averages for the entire year of 2006. The maximum geopotential and zonal wind values are calculated for each variable respectively in West Africa and East Africa into the Arabian Peninsula. The results indicate how the LWM_W and LWM_E intensities are dependent on the strength of the anticyclonic induced pressure gradient. Figure 2.8a shows strong positive correlation (.80) of the Saharan high and LWM_W. The intensity of the LWM_W fluctuates with the Saharan high intensity. Since the Saharan high and LWM_W are present all year long, the variation of intensity occurs simultaneously. The LWM_E and Arabian high are not present all year. The correlation (.70) of the LWM_E and Arabian high is weak throughout the year, until May. In Figure 2.8b the LWM_E has an increase in strength, as well as the Arabian high during mid-summer and begins to decrease in the fall.

The formation and evolution of the LWM_E and Arabian high are depicted in the monthly averages of 2006 using 600 mb zonal winds and streamfunction (Figure 2.9). During the winter month of January, the sub-tropical high stretches from the Africa to India with a jet maximum located to the south of each anticyclonic center. Over Africa, the LWM_W exists between 5°N and 10°N with no presence of the LWM_E in East Africa or Arabian high over the Arabian Peninsula. In March and April, the Arabian high begins its formation stage.

In May, the Saharan high center is displaced poleward and a secondary anticyclonic center forms over the Arabian Peninsula along with the $LWM_{E,}$ which reaches the mature stage of the Arabian high. The co-existence of the LWM_E and Arabian high indicates that both systems are formed during this time.

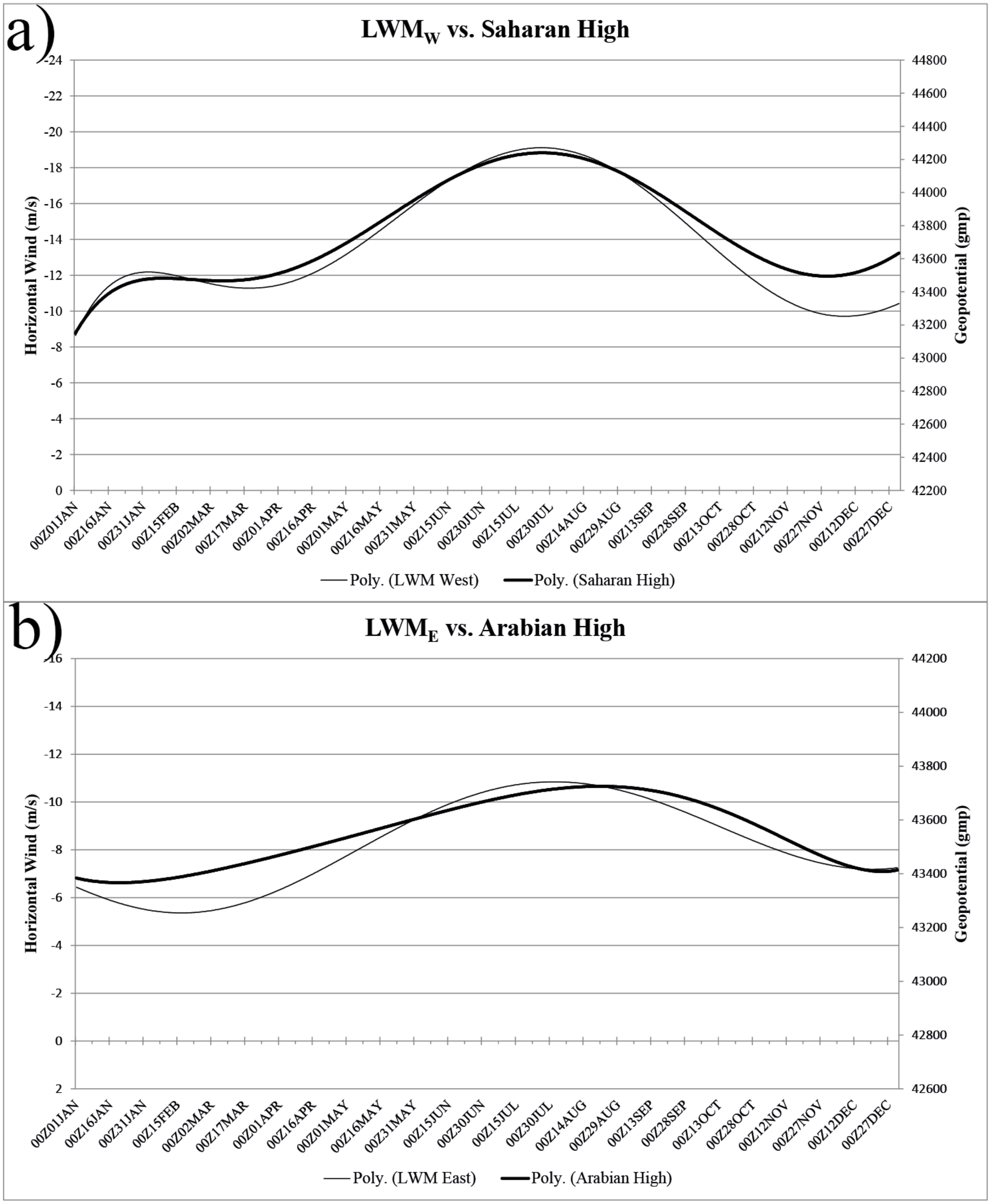

Figure 2.8. 2006 daily averaged curve of maximum zonal wind (m s^{-1}) [thin line] and geopotential (gmp) [bold line] and for (a) the Saharan high/LWM_W and (b) the Arabian high/LWM_E.

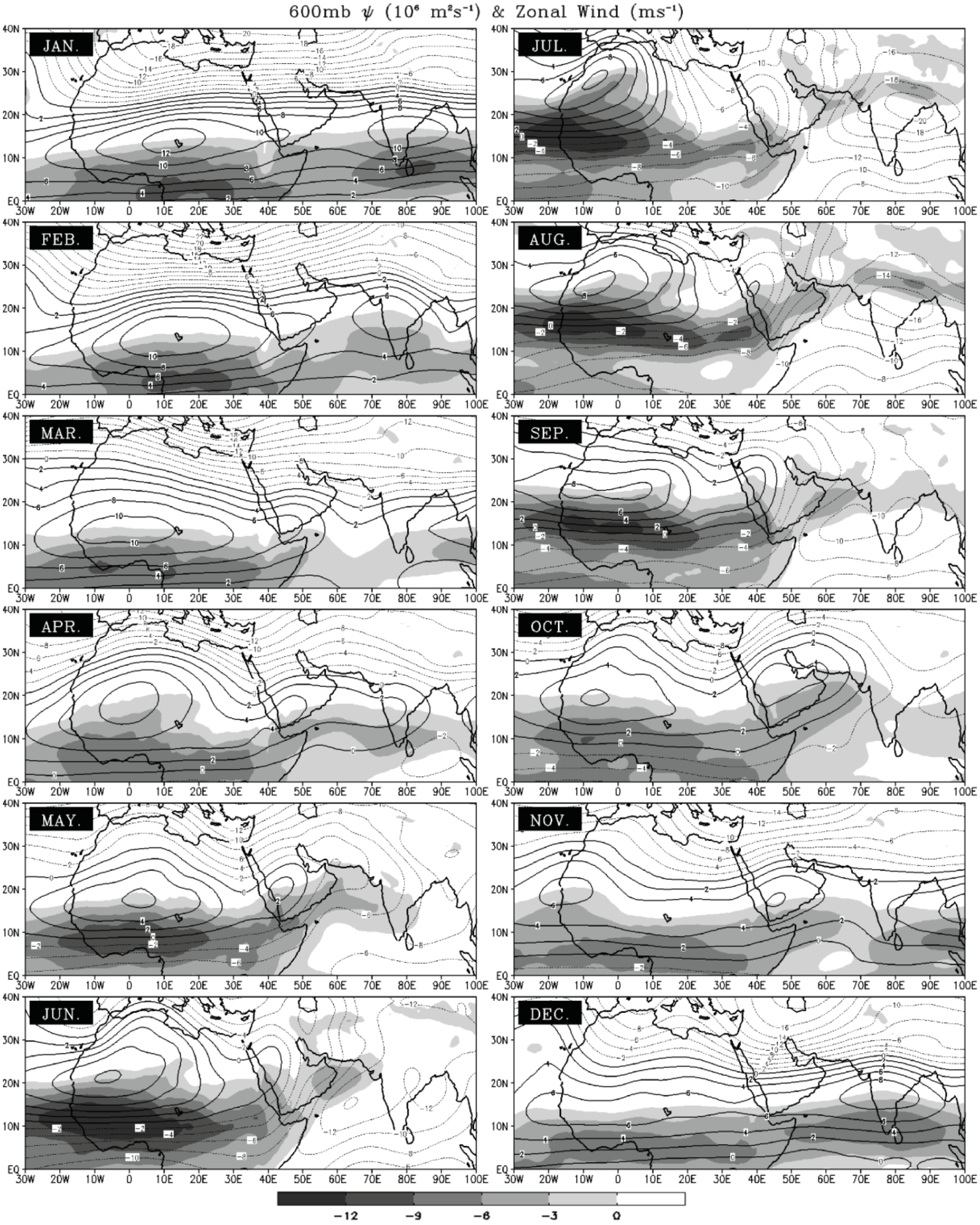

Figure 2.9. 2006 monthly averages of 600 mb streamfunction ($m^2\ s^{-1}$) contours and zonal wind ($m\ s^{-1}$) shaded every 3 $m\ s^{-1}$.

In June, the Saharan high and LWM_W occupies most of North Africa while stretching into East Africa and part of North Arabia. There is no LWM_E present during June and July according to the monthly averages of streamfunction and zonal wind. This is due to the Arabian high being very weak and unable to produce a geopotential gradient to form the LWM_E. In August, a second anticyclonic center develops over the Arabian Peninsula. The development of the Arabian anticyclonic center induces the LWM_E by forming from the meridional geopotential gradient. By October, the Saharan high is weakened along with the LWM_W and the Arabian high is dominant over the Arabian Peninsula.

The Saharan high/LWM_W and Arabian high/LWM_E in August are depicted by a Hovmoller diagram every 6 hours (Figure 2.10). The latitudinal cross section for geopotential and zonal wind are based on their location during August 2006 (Figure 2.9). The AEJ is on the southern rim of the subtropical anticyclones, so the latitudinal cross section of geopotential is at 27°N (Figure 2.10a) and the latitudinal cross section of zonal wind is at 17°N (Figure 2.10b). In August, the highest geopotential values are located between 20°W and 20°E, which is directly related to the Saharan high and between 40°E and 50°E, which is directly related to the Arabian high. In between these highs is a trough that is associated with the sub-tropical westerly jet stream over the Mediterranean region (Gaetani 2011). Observations from the Hovemoller diagram of geopotential, the Saharan high shows advection between August 11 and August 21. The zonal wind in Figure 2.10b can be compared with Figure 2.10a to see the relationship of the easterly winds and the high pressure systems. On a 6 hourly time scale, the LWMs can respectively be depicted in the same region of the high pressure systems. Since the Hovmoller diagram does not consist of any averaging, the LWMs reach zonal magnitudes higher than the climate average presented in section 2.3.1. The LWM_W has a zonal wind speed of 16 m s^{-1} or greater and the LWM_E has a zonal wind speed of 10 m s^{-1} or greater.

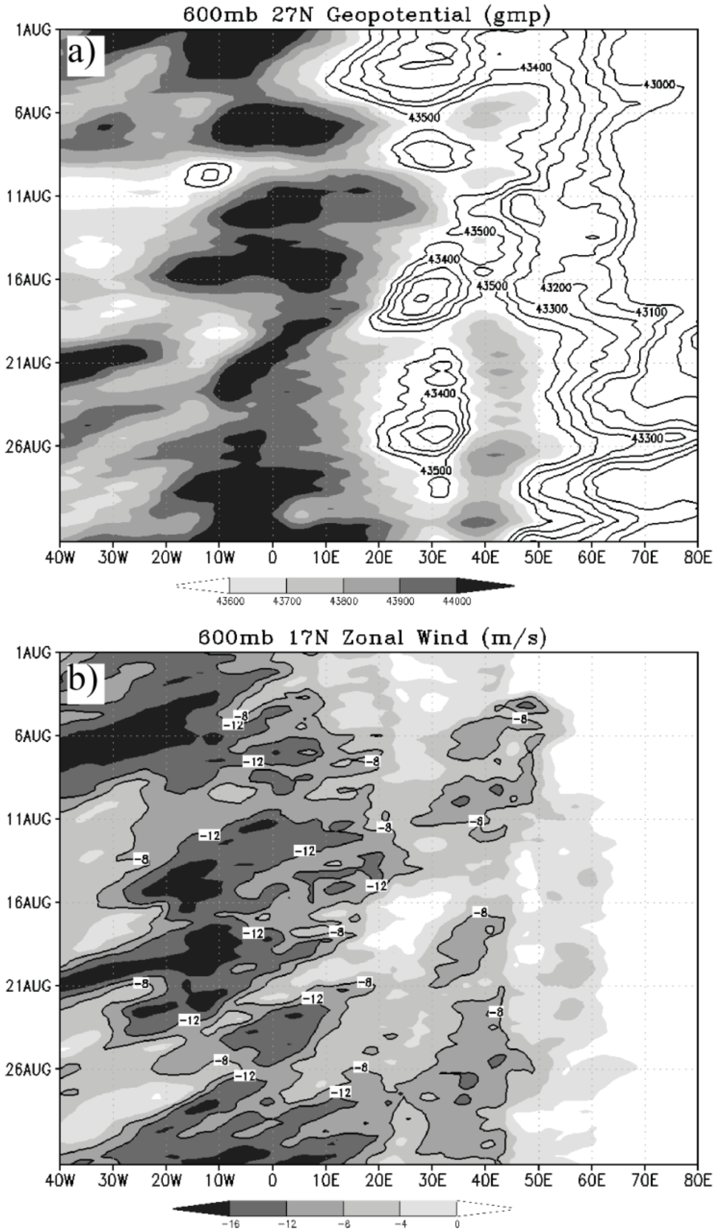

Figure 2.10. August 2006 Hovmoller diagram of (a) geopotential (gmp) at 27°N shaded between 43600 and 44000 every 100 gmp and contoured between 43000 and 43500 every 100 gmp and (b) zonal wind (m s^{-1}) at 17°N shaded -16 to 0 every -4 m s^{-1} and contours for 12 m s^{-1} and 8 m s^{-1}.

2.4 Summary and Discussion

The African Easterly Jet was analyzed for the month of August between 1976 and 2010 as well as 2006 as a case study to demonstrate a second maximum core located in East Africa centered around (15^{o}N, 35^{o}E). Once this maximum was identified, there was a series of examinations that explained the dynamical interactions of the LWM$_E$ and the East African synoptic circulations. Similar to the LWM$_W$ found and discussed in previous studies, the LWM$_E$ exhibited very similar mechanisms in formation and maintenance. The LWM$_E$ is located south of the Arabian high much like the LWM$_W$ located south of the Saharan high. The increased intensity of the LWMs associated with AEJ is due to the maximum meridional geopotential gradient from the Saharan and Arabian highs, which causes the AEJ to be mainly geostrophic. This was explained utilizing the thermal wind relationship to differentiate between the LWM$_W$ and LWM$_E$.

The formation and maintenance of the Saharan and Arabian highs were also discussed. From the east-west circulation, there were two distinct divergence flows in the mid-levels that were over Africa and the Arabian Peninsula. The upward vertical motion is associated with the ITF heating in which the Saharan and the Arabian thermal lows are located. The rising of warm air converges with the sinking cooler air forming divergence centers over Africa and the Arabian Peninsula. This differential heating from the divergent centers help maintain the anticyclones.

The LWMs and anticyclonic systems were investigated on a smaller spatial time scale for the year 2006 using monthly averages. The formation and evolution of the Arabian high begins in March reaching peak intensity in May, August, and October and the LWM$_E$ is at maximum intensity during August.

The presence of the LWM_E can offer better understanding of rainfall distribution and interactions with easterly wave maintenance and propagation in East Africa. More research is needed to understand this interaction, such as high resolution numerical modeling. Climate variability of the Arabian high and LWM_E can also be investigated with the El Nino Southern-Oscillation (ENSO) to determine weather changes over East Africa.

CHAPTER 3

Variability of the Subtropical Highs, African Easterly Jet and Easterly Wave Intensities over North Africa and Arabian Peninsula in Late Summer

3.1 Statement of Problem

In this research, we plan to extend the study of Spinks et al. (2014) to investigate the yearly variability of AEJ, LWMs, easterly waves and AEWs in their intensities over North Africa and the Arabian Peninsula during the same period. The sensitivities of these features to El Nino-Southern Oscillation (ENSO) will be studied. Points of interest include displacements of the LWMs and anticyclonic systems, structure of the AEJ, and relative vorticity intensities.

3.2 Data

In this study we will use the ECMWF-interim reanalysis data with a spatial resolution of 0.75° x 0.75° on a global grid for August between 1979 and 2010 (Dee et al. 2011). With this data set, the variability and structure of the Saharan and Arabian highs, LWMs, and vorticity fields can be analyzed with climatological means. The Multivariate ENSO Index (MEI) (Wolter and Timlin 1987, 1993, 1998, and 2011) will be used to extract values and make composites of the synoptic situations over Africa for ENSO and Non-ENSO seasons. Unlike other ENSO indices that use only SST, the MEI, as proposed by the National Oceanic and Atmospheric Administration (NOAA) Earth System Research Laboratory (ESRL), uses six major observed variables over the tropical Pacific. These six variables are: sea-level pressure (P), zonal (U) and meridional (V) components of the surface wind, sea surface temperature (S), surface air temperature (A), and total cloudiness fraction of the sky (C). In addition, the MEI uses bimonthly values, so the indices for July-August and August-September were averaged to obtain the ENSO index for August.

3.3 Results

3.3.1 Variability of Subtropical Highs, LWMs, and Easterly Waves. At mid-troposphere, such as 600 mb, the Saharan and Arabian highs can be depicted with streamfunction (ψ) to show circulation (Figure 3.1a). To the south of the highs, there exists an AEJ axis with two embedded LWMs in East and West Africa, respectively, which can be illustrated by the zonal wind field (Figure 3.1b). Since the easterly waves propagate along the southern side of the AEJ axis, zeta (ζ) is used to show the relative vorticity intensity over North Africa (Figure 3.1c). Since the streamfunction and zonal wind fields are used to identify the maxima for the Saharan and Arabian highs and LWMs, respectively, the mean, variance and displacement for these maxima can be seen in Tables 1 and 2. To obtain the averages for the subtropical highs and LWMs, a regional domain in West and East Africa was set up to calculate maximum values.

The Saharan high has a mean streamfunction value of 9.1 $m^2 s^{-1}$ with a variance of 1.9 for the month of August (Table 1 and Figure 3.1d). Most of the streamfunction variance occurs just north of the sub-tropical highs and over of the Mediterranean Sea which is associated with a mid-level subtropical jet stream. In the lower latitudes the highest variance can be seen in central North Africa and over the northern and southern portions of the Arabian Peninsula. On average the Saharan high is located at (28.4°N, 4.7°W). The longitudinal and latitudinal variances are 8.8° and 2.8°, respectively. The associated $LWM_{W,}$ which is located to the south of the Saharan high, has a zonal wind speed maximum of -13.5 ms^{-1} with a variance of 0.9. The highest variability of the AEJ exists over central North Africa (Table 2 and Figure 3.1e). On average, the LWM_W maximum is located at (16.2°N, 12.3°W). The longitudinal variance of the LWM_W is rather large because of displacement being between 20°W and 0°. Those anomalous years when the LWM_W is around 0° include 1986, 2000, 2002, and 2003. Exclusion of those years, the longitudinal variance of the LWM_W would decrease to 4.9°. The latitude of the LWM_W can reach as high as 18°N and as low as 13.5°N during August.

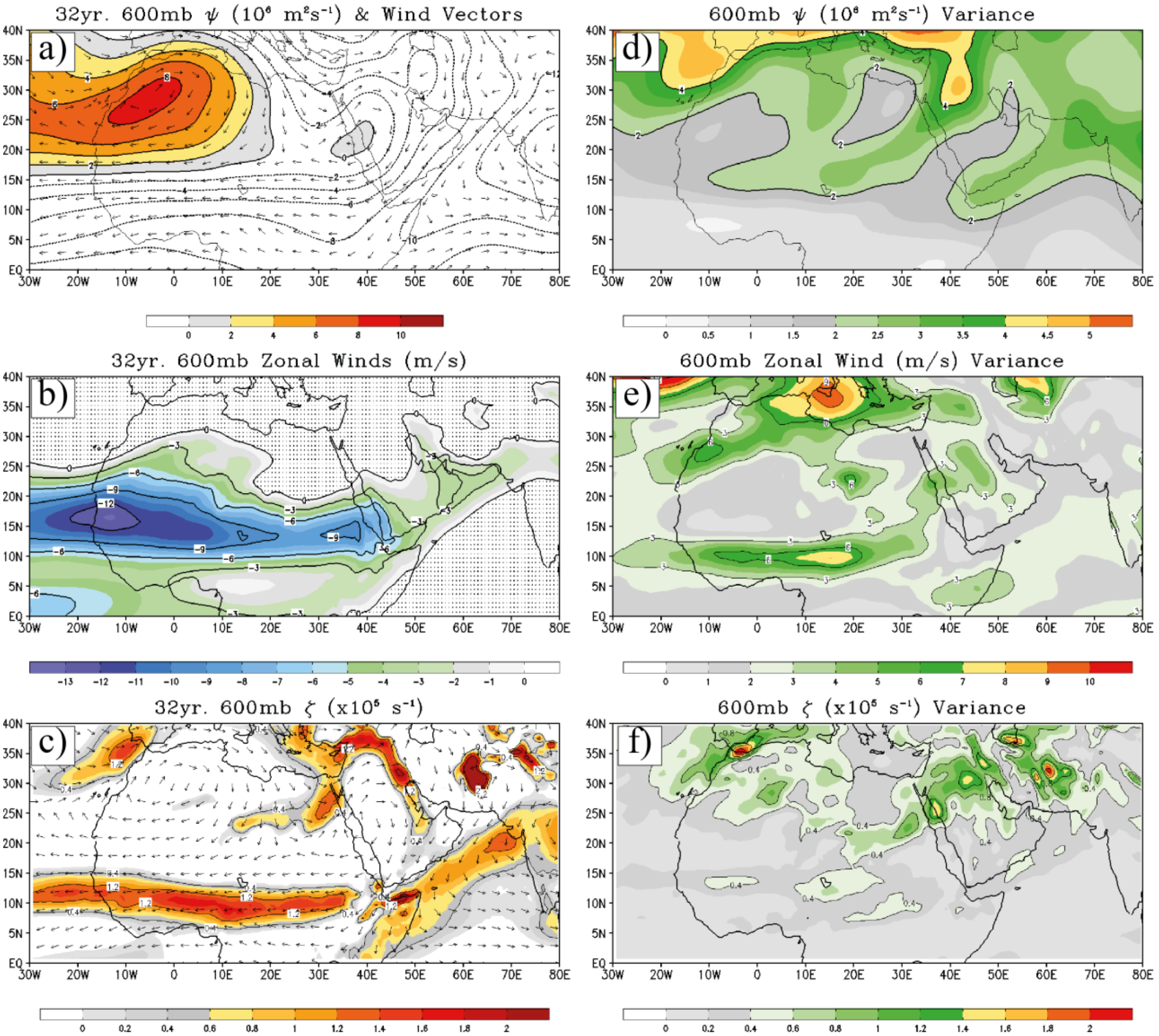

Figure 3.1. Averaged 32-year (1979-2010), 600-mb fields for August: a) streamfunction ($m^2\,s^{-1}$) and wind vectors, b) zonal wind ($m\,s^{-1}$), c) relative vorticity (s^{-1}) and wind vectors, d) streamfunction variance, e) zonal wind variance, and f) relative vorticity variance.

The Arabian high has a mean streamfunction value of 0.7 $m^2\,s^{-1}$ with a variance of 2.2 (Figure 3.1d) and averaged location at (21.9°N, 38.1°E). The longitudinal and latitudinal variances are 4.2° and 4.4°, respectively. The associated LWM_E, which is to the south of the

Arabian high, has a mean of -9.9 ms^{-1} with a variance of 1.9 (Table 2 and Figure 3.1e). Compared to the LWM$_{\mathrm{W}}$, the LWM$_{\mathrm{E}}$ does not vary as much in the longitudinal (35.7° E, 9.4°) and latitudinal (13.8° N, 0.8°) directions. The Arabian high and LWM$_{\mathrm{E}}$ are much smaller in size and weaker in intensity. The Arabian high and LWM$_{\mathrm{E}}$ are semi-permanent features in which Spinks et al. (2014) which investigated the evolution of these systems for the entire year of 2006. Unlike the Saharan high and LWM$_{\mathrm{W}}$, the Arabian high and LWM$_{\mathrm{E}}$ are formed in March and are matured by May. From June through late July, the systems weaken substantially while the Saharan high dominates most of North Africa, especially in West Africa. In August, the Arabian high and LWM$_{\mathrm{E}}$ can be seen in a developing or mature stage where the LWM$_{\mathrm{E}}$ is intense in East Africa.

Table 1

August 1979-2010 average and variance of maximum streamfunction values associated with the Saharan and Arabian high in East and West Africa.

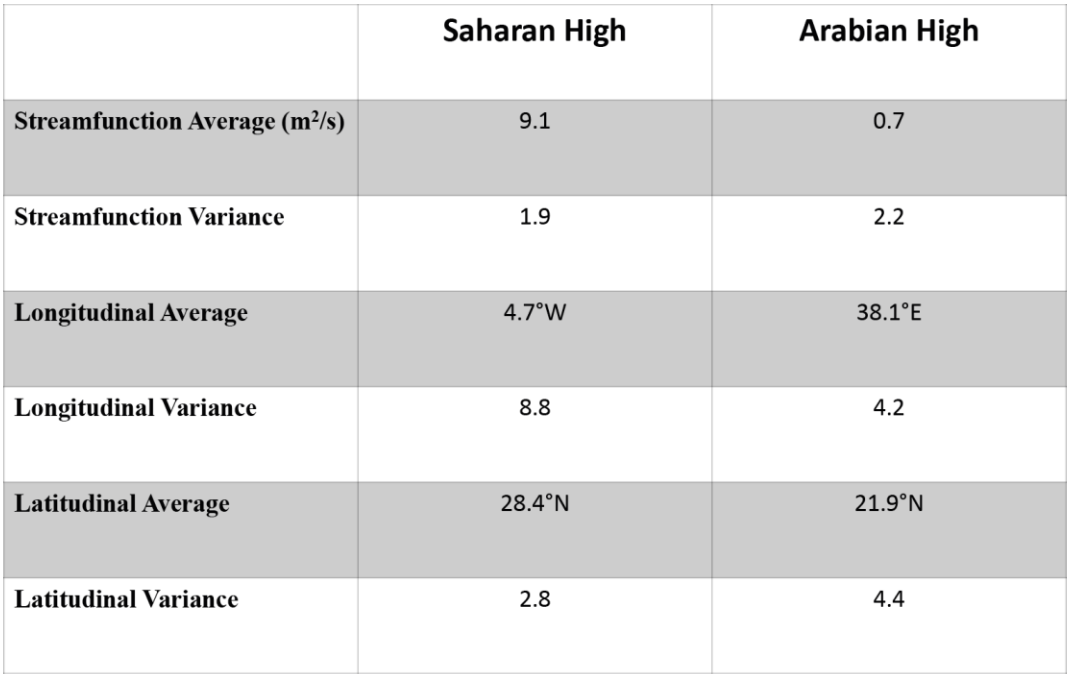

	Saharan High	Arabian High
Streamfunction Average (m^2/s)	9.1	0.7
Streamfunction Variance	1.9	2.2
Longitudinal Average	4.7°W	38.1°E
Longitudinal Variance	8.8	4.2
Latitudinal Average	28.4°N	21.9°N
Latitudinal Variance	2.8	4.4

Table 2

August 32-year (1979-2010) average and variance of maximum zonal winds associated with the LWM_W *and* LWM_E.

	LWM_W	LWM_E
Zonal Average (m/s)	-13.5	-9.9
Zonal Variance	0.9	1.9
Longitudinal Average	12.3°W	35.7°E
Longitudinal Variance	23.8	9.4
Latitudinal Average	16.2°N	13.8°N
Latitudinal Variance	1.3	0.8

The significance of the existence of the LWM_E would aid the propagation and maintenance of easterly waves coming from the Arabian Peninsula into East Africa. Lin et al. (2013) explored the genesis of an easterly wave associated with the pre-Tropical Storm Debby AEW over the Arabian Peninsula. Propagation of this wave is by the easterly wind flow at 600 mb and was enhanced due to orographic forcing from the Ethiopian Highlands and the LWM_E. Figure 3.1c depicts the relative vorticity field over Africa and the Arabian Peninsula. This field only serves as an explanation of averaged easterly wave intensity and does not account for the number of easterly waves across North Africa. In addition, this relative vorticity region is an indicator of easterly wave propagation paths south of the AEJ and easterly wind flow. The most intense region of vorticity can be seen over central Africa between 0° and 10°E. The vorticity field remains intense into East Africa and decreases slightly into the Arabian Peninsula. There exists a vorticity maximum at 10°N between 40°E and 50°E, which could be a significant feature for a possible wave genesis location. Other features from the vorticity field include the trough located between the Saharan and Arabian highs and vorticity field on the east quadrant of the Arabian high. Analyzing the variance in Figure 3.1f depicts the greatest variance of easterly wave intensities are at 5°W and 10°E to 35°E. Over Arabian Peninsula, the variance associated with the easterly wave genesis region (15°N, 55°E) is also high for the easterly wave propagation region.

The Saharan high, Arabian high, meridional geopotential and temperature gradients are the biggest role players in the intensity of the AEJ and its associated LWMs. By performing a correlated calculation of the intensities of the LWMs and its associated dynamical processes it can determine which process has the biggest influence on the intensity. Figure 3.2 is the LWM_W zonal intensities versus the meridional geopotential gradient (Figure 3.2a), meridional temperature gradient (Figure 3.2b), and streamfunction (Figure 3.2c) between 1979 and 2010 for the month of August. The correlations between these variables are relatively high which is to be expected because each variable contributes to the intensity of the LWM_W and overall AEJ. The streamfunction (Saharan high) shows a correlation with the LWM_W of $r = 0.59$, the meridional geopotential gradient with $r = 0.80$, and the meridional temperature gradient with $r = 0.69$. Since the LWM_W is mainly geostrophic it's not surprising that the meridional geopotential gradient illustrates the highest correlation. There are also noticeable years where the LWM_W is very strong (LWM_W anomaly > 1.0), which includes 1984, 1994, 1998, 2000, 2007, and 2009.

The correlations for the LWM_E are much higher than the LWM_W (Figure 3.3). The streamfunction shows a correlations of $r = 0.80$, the meridional geopotential gradient with $r = 0.95$, and the meridional temperature gradient with $r = 0.77$. Similar to the LWM_W, the meridional geopotential gradient has the highest correlation to the LWM_E intensity. Noticeable years where the LWM_E intensity is very strong ($LWM_E > 1.0$) includes 1995, 1996, 1998, 1999, 2000, 2001, and 2010. Prior to 1995, the LWM_E is either neutral in intensity or very weak. Explanation of this could be due to ENSO. The Arabian high had its strongest year during this study in 1995 with a positive anomaly of 2.8, which is positively correlated with the LWM_E intensity. The two years that stand out most for the AEJ's varying intensity were the strong ENSO year in 1997 and Non-ENSO in 1998 for August.

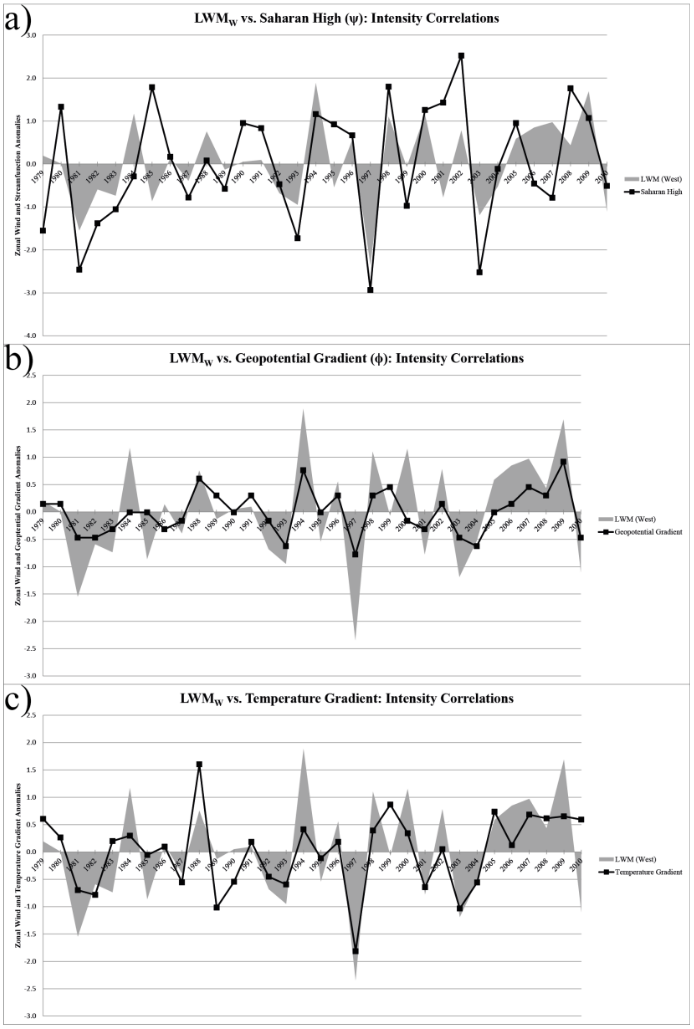
a) LWM_W vs. Saharan High (ψ): Intensity Correlations

b) LWM_W vs. Geopotential Gradient (ϕ): Intensity Correlations

c) LWM_W vs. Temperature Gradient: Intensity Correlations

Figure 3.2. Zonal wind maximum intensity (shaded) correlations to (a) meridional geopotential gradient, (b) meridional temperature gradient, and (c) streamfunction (Saharan high) intensity in West Africa for August during 1979-2010.

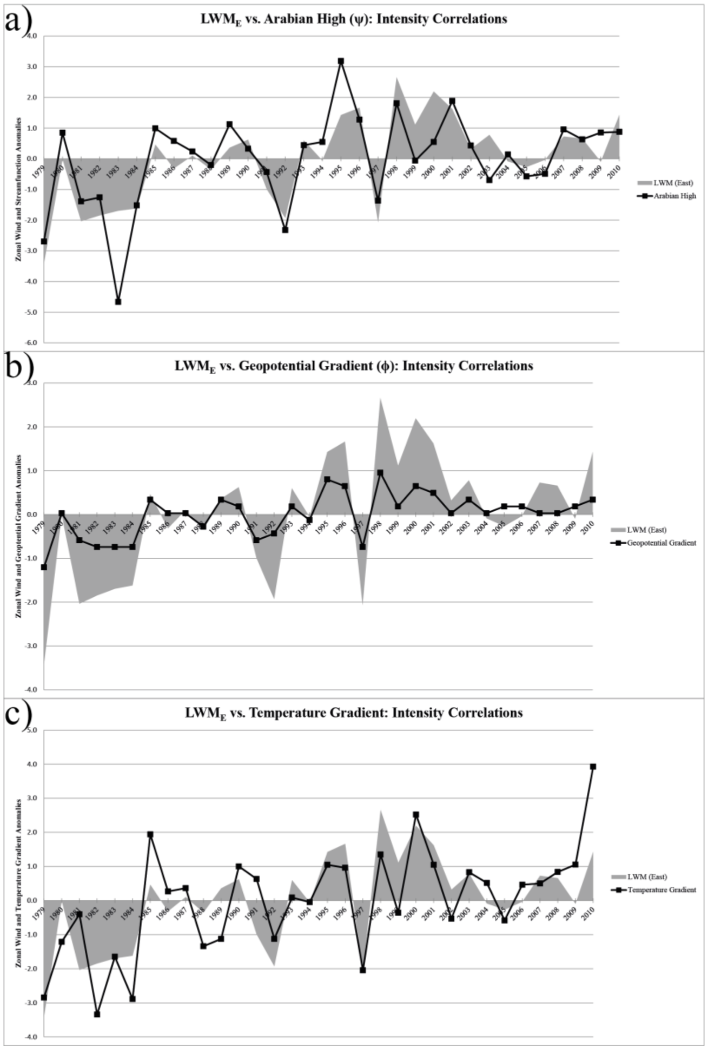

Figure 3.3. Zonal wind maximum intensity (shaded) correlations to (a) meridional geopotential gradient, (b) meridional temperature gradient, and (c) streamfunction intensity in East Africa for August during 1979-2010.

3.3.2 ENSO Composite and Analysis of Subtropical Highs, LWMs, and Easterly Waves

3.3.2.1 MEI Index. Since the variance has been established in the previous section, it is important to look into when the subtropical highs, LWMs, and easterly wave intensities are weak or strong. In other words, we are particularly interested in the effects of ENSO on the intensities of these synoptic systems. This can be accomplished by using the MEI (Figure 3.4). ENSO years are generally represented by the MEI index when it is greater than 0.5 and the Non-ENSO years are well represented when MEI index less than -0.5. Notable ENSO years (MEI > 1) for August are 1982, 1986, 1987, 1993, and 1997, while notable Non-ENSO years (MEI < -1) occurred in 1988 and 2010. Based on the 32 years of observations from the MEI, the ENSO phase is generally positive for August.

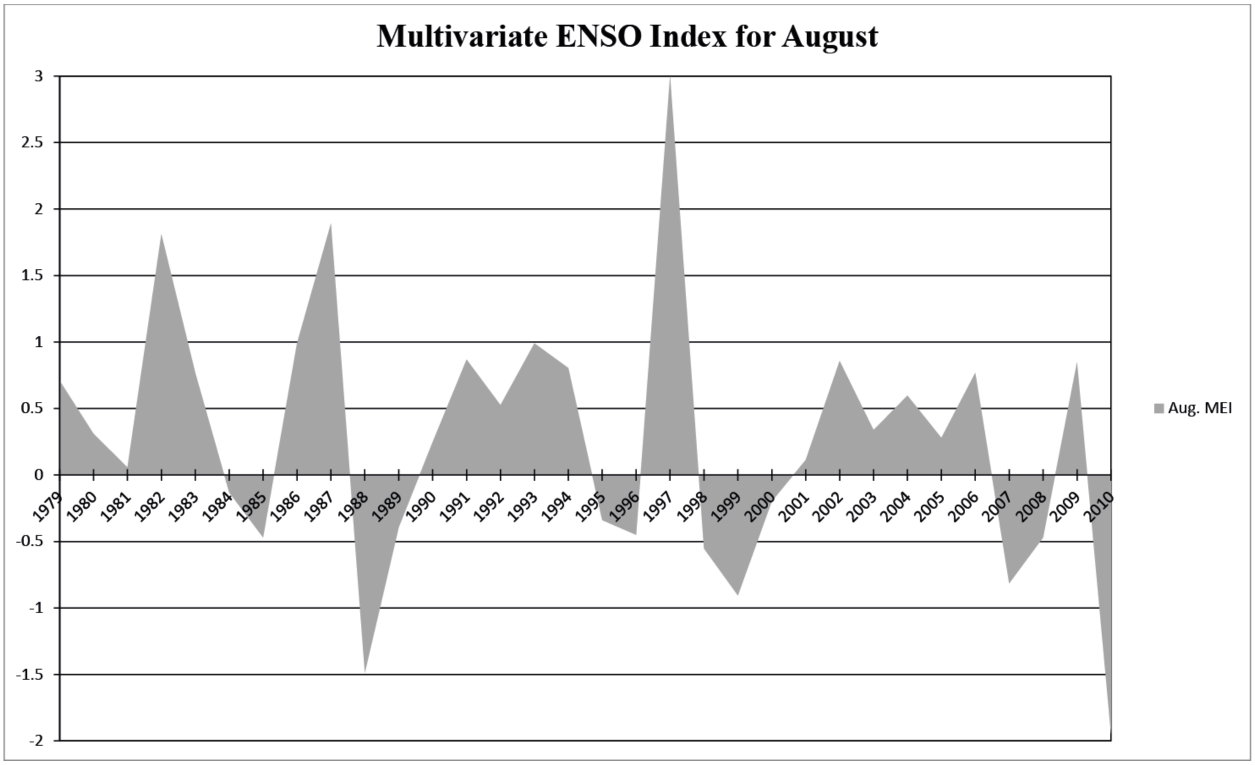

Figure 3.4. Multivariate ENSO Index for August during 1979-2010.

3.3.2.2 ENSO Composites. Figure 3.5 illustrates the ENSO variability of the Saharan and Arabian high using streamfunction. Results from this composite analysis reveal that these respected anticyclonic systems strengthen during negative ENSO phases and weakens during positive ENSO phases. The most noticeable change between phases comes from the Arabian high, which has a higher variance than the Saharan high at 2.2. The displacement of the anticyclonic system is slightly higher in latitudes, but not significant in change. The strengthening of the Arabian high is also an increase in pressure, which is a direct influence of the $\mathrm{LWM_E}$.

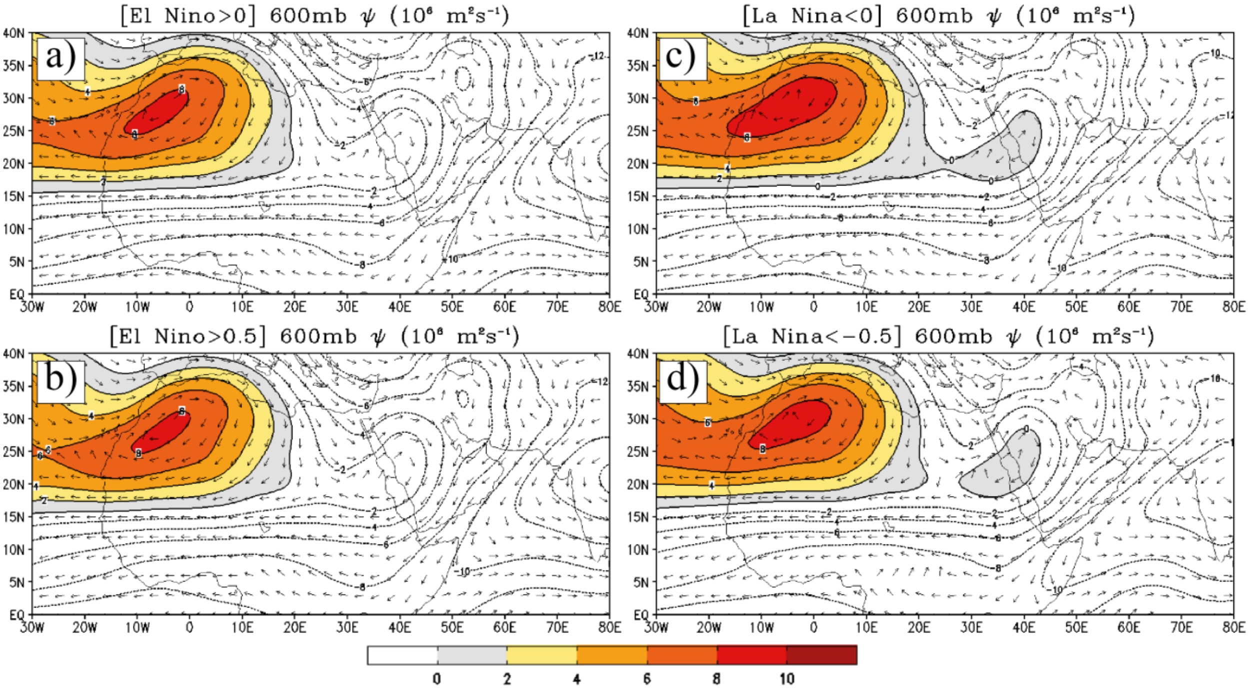

Figure 3.5. Composites of streamfunction at 600 mb using the MEI for ENSO: (a) MEI > 0 (all positive years), (b) MEI > 0.5 (ENSO years), (c) MEI < 0 (all negative years), and (d) MEI < -0.5 (Non-ENSO years).

Figure 3.6 depicts the ENSO composite of the AEJ. Similar to the highs, the AEJ's intensity increases (decreases) to negative (positive) ENSO years. The zonal wind speeds of the $\mathrm{LWM_W}$ do not vary in intensity much between ENSO years, but the $\mathrm{LWM_E}$'s higher zonal variance shows an increase from 8 to 10 m s^{-1} during extreme ENSO and Non-ENSO years, respectively. The structure of the AEJ also changes between ENSO years. During extreme ENSO years, the AEJ is weaker than average (Figure 3.1b) and broader in latitude. The zonal wind contours show a weaker gradient between 10°N and 15°N. The $\mathrm{LWM_E}$ is present and weak compared to the averaged intensity. During extreme Non-ENSO years, both LWMs increase in intensity as well as the overall intensity of the AEJ. The gradient of the zonal winds are strong between 10°N and 15°N, mainly due to the presence of the westerly jet into the mid-levels located at (5°N-10°N, 10°E-20°E). The LWM_W expands in size, but there is no significant change in intensity.

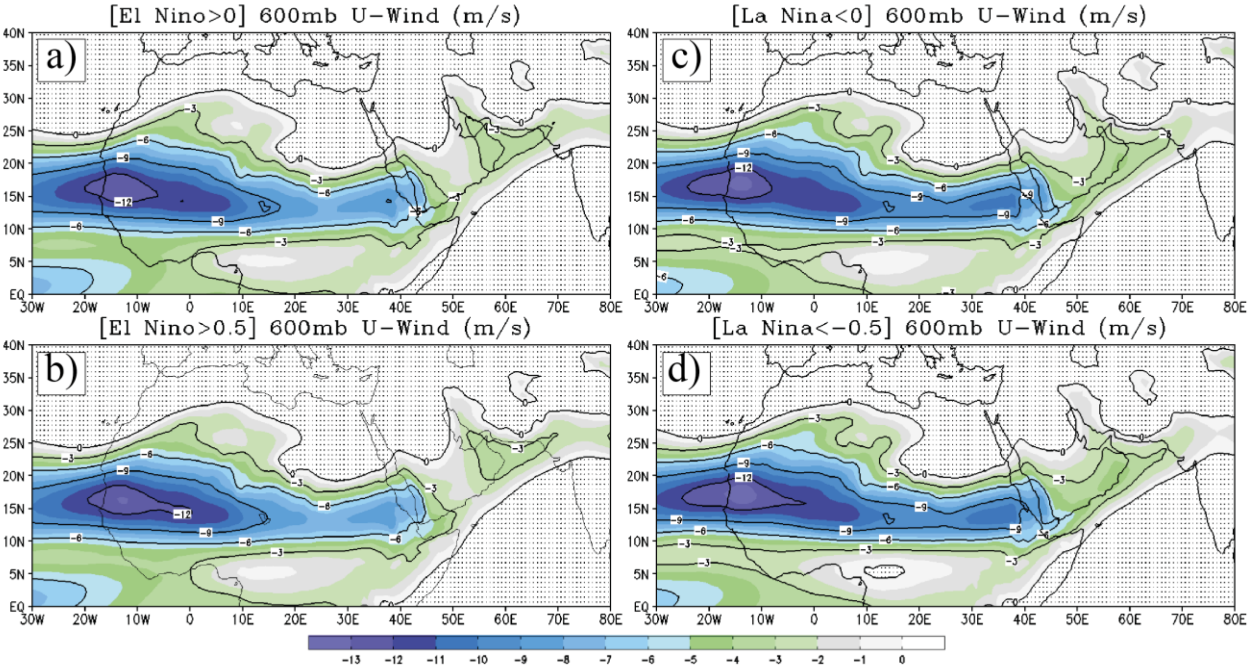

Figure 3.6. Composites of zonal wind at 600 mb using the MEI for ENSO: (a) MEI > 0 (all positive years), (b) MEI > 0.5 (ENSO years), (c) MEI < 0 (all negative years), and (d) MEI < -0.5 (Non-ENSO years).

The AEJ's 3 m s^{-1} zonal wind contour does not extend into the southern Arabian Peninsula during extreme ENSO seasons (Figure 3.6c), but does during extreme Non-ENSO seasons (Figure 3.6d). The significance of the zonal wind increase over southern Arabia during extreme Non-ENSO season means a strong positive zonal gradient ($\partial u / \partial y > 0$) will increase vorticity intensity ($\zeta = \partial v / \partial x - \partial u / \partial y$). This increase of the zonal gradient during extreme Non-ENSO years is important for easterly wave propagation over the Arabian Peninsula.

The relative vorticity composite for ENSO years can be illustrated in Figure 3.7. The vorticity field (8°N-15°N) shows significance in intensity variability during extreme ENSO and Non-ENSO years across West Africa, East Africa and the Arabian Peninsula. It is noteworthy that the intensity of the relative vorticity field does not mean that there is an increase of the number of easterly waves.

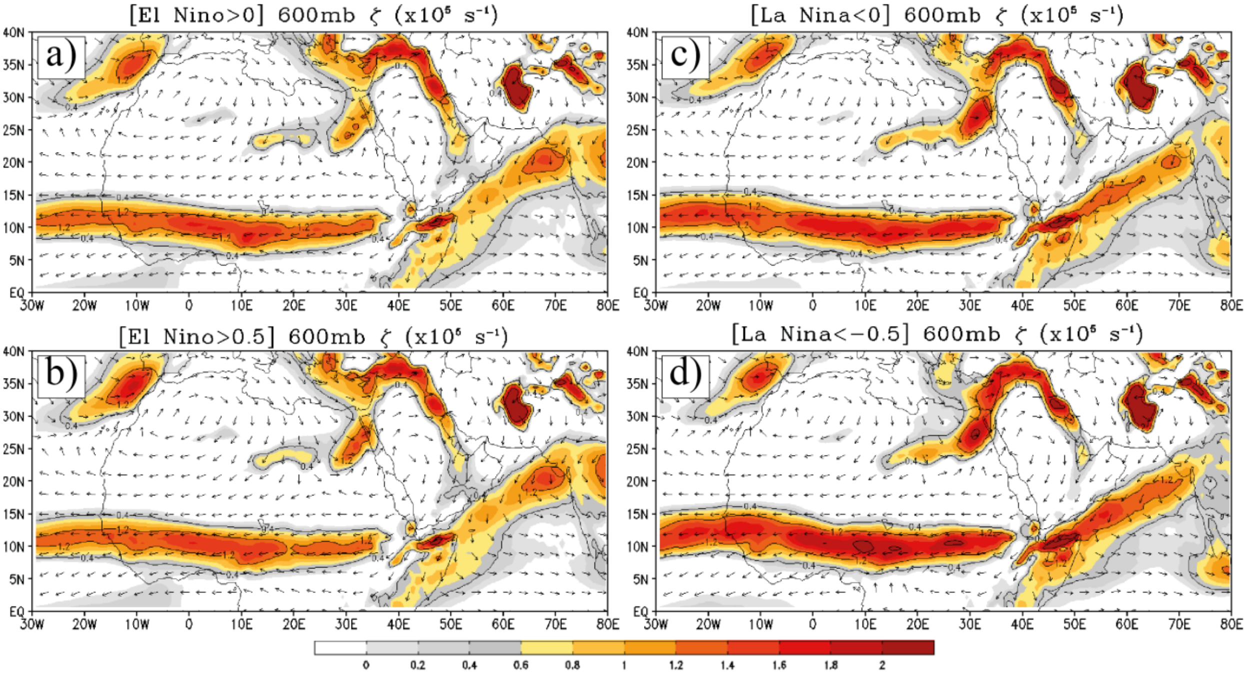

Figure 3.7. Composites of relative vorticity at 600 mb using the MEI for ENSO: (a) MEI > 0 (all positive years), (b) MEI > 0.5 (ENSO years), (c) MEI < 0 (all negative years), and (d) MEI < -0.5 (Non-ENSO years).

This composite analysis simply illustrates that easterly wave intensity will increase (decrease) during negative (positive) ENSO years. During extreme ENSO years, the vorticity field shows a decrease in intensity from the average (Figure 3.1c). The vorticity field over the Arabian Peninsula shows the most decrease in intensity compared to the average. With the zonal winds of the AEJ, particularly the 3 m s^{-1} contour is not present over southern Arabia; easterly wave intensity will be inhibited slightly. The vorticity field in East Africa also shows a decrease in intensity, especially south of the region where the LWM_E is located.

During extreme Non-ENSO years, the vorticity field increases in intensity significantly from that average. Vorticity in West Africa is stronger over the Guinea Highlands as well as the lee side of the mountains. The larger increase in vorticity strengthening is over Central Africa between 0° and 20°E. This is due to the presence of the westerly jet in mid-levels (Figure 3.4) in extreme Non-ENSO years. With the subtropical anticyclonic systems strengthening, which influences the magnitude of the AEJ and the presence of the westerly jet, the vorticity will be strengthened over Central Africa. The variance from Figure 3.1e and f illustrates the highest variance to be over Central Africa for the zonal winds and vorticity field. The vorticity field is also strengthened in East Africa, especially over the region south of the LWM_E. Into the Arabian Peninsula the vorticity field shows the increase of vorticity genesis area proposed by Lin et al. (2013). The positive and negative ENSO years reveal similar variances as the extreme years except the intensities are slightly lower for the vorticity field.

3.3.2.3 East-West Vertical Circulation Cell. So far in this research it has been established that during extreme ENSO (Non-ENSO) years the subtropical highs, LWMs, and vorticity fields decreases (increases) in strength respectively. The vorticity field decrease (increase) is due to weaker (stronger) zonal gradient of the AEJ. The intensity of the LWMs decrease (increase) with the weakening (strengthening) of the subtropical highs induced meridional geopotential gradient. The temperature is accounted for in its relation to AEJ intensity, but structure and existence of the LWMs are due to the meridional geopotential gradient since the AEJ is mainly geostrophic. The meridional temperature gradient, i.e. the baroclinicity, serves the formation mechanism to the AEJ (Thorncroft and Blackburn 1999, Wu et al. 2009). Chen (2005) established that the LWM_W decreases (increases) with the Saharan high and Spinks et al. (2014) established that the LWM_E decreases (increases) with the Arabian high. The next question is what causes the decrease (increase) in the strength of the subtropical anticyclonic systems?

The Saharan and Arabian highs are both maintained mainly by the east-west differential heating. Divergent centers over North Africa and the Arabian Peninsula are produced by the thermal heating which creates a low near surface and forces the air to rise and converge with the sinking cooler air from the upper atmosphere. Figure 3.8 illustrates the east-west circulation and vertical motion field over North African and the Arabian Peninsula along a vertical cross section of 20°N.

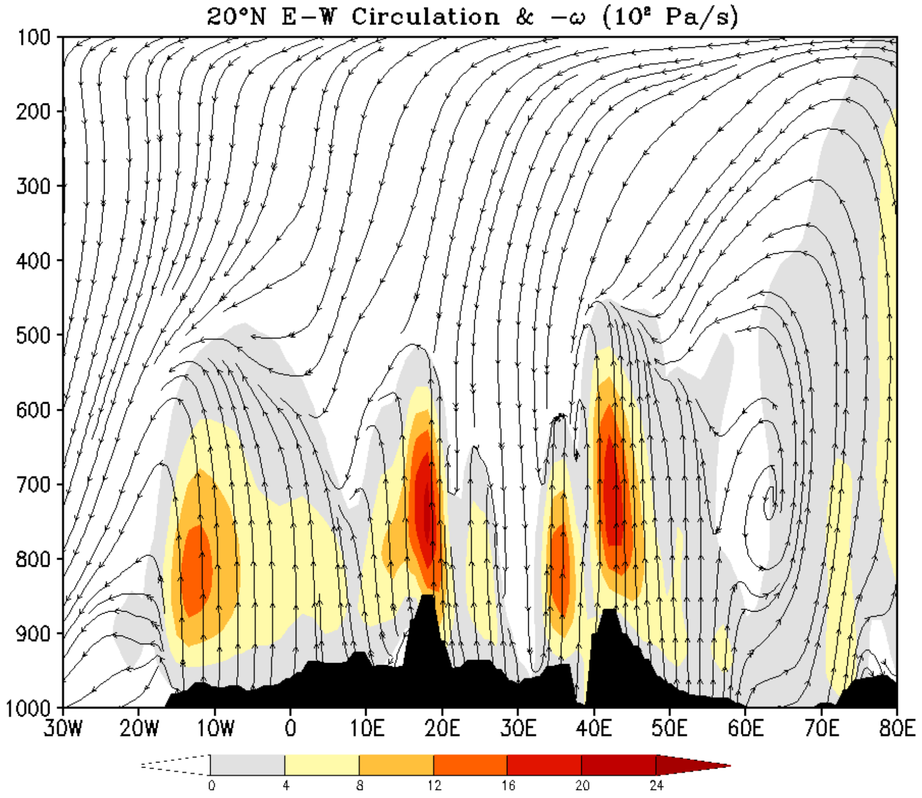

Figure 3.8. Averaged vertical cross section at 20°N of zonal wind and $-\omega$ (10^2 Pa s^{-1}) for August during 32-year (1979-2010) period.

The latitude 20°N was chosen because the strongest vertical upward motions in the layer between 925 and 825 mb were found there based on Fig. 1c from Spinks et al. (2014). The strongest vertical motions are located over the mountain ranges across North Africa and the Saharan and Arabian thermal lows. The divergence is seen in the mid-levels, such as in the layer of 700 to 500 mb. This was also illustrated from the velocity potential field at 600 mb in Chen (2005) and Spinks et al. (2014) which depicted the divergent centers associated with the strong convergences of the upward and downward motions. Between 60°E and 70°E, there is a vertical circulation cell present. This cell's formation is from the low-level westerlies associated with the Indian Ocean subtropical high, the intense upward vertical motion associated with the Asian monsoonal low, the upper-level tropical easterly jet, and the sinking cooler air from the northerlies over North Africa. The tropical easterly jet is in accelerating phase east of about 75°E where an upward branch of east-west Walker cell is located and in decelerating phase west of it (Chen 1982, Sathiyamoorthy et al. 2007). This cell formation can be clearly illustrated from Fig. 1 of Spinks et al. (2014). Our question is: Does the presence of this cell and its associated east-west circulation patterns have an effect on the intensity of the Saharan and Arabian high since both systems rely on the east-west differential heating?

It is noticeable from Figure 3.1d-f and Tables 1 and 2 that the highest variability of intensity from the subtropical highs, AEJ, and relative vorticity occurs in East Africa and Central Africa. West Africa does not experience the same variation of intensity. The variation of intensity over East Africa and the Arabian Peninsula can be explained by the presence of the east-west vertical circulation cell between 60°E and 70°E (Figure 3.9). Analyzing the positive ENSO years, the east-west circulation cell is no longer present. This is due to the reduced zonal wind speeds from the tropical easterly jet in the upper atmosphere and the low-level westerlies associated with the high in the Indian Ocean. The divergence field associated with the convergence of vertical motions in the mid-atmosphere does vary as much. Since the winds coverage over North Africa at 20°N, then the upward vertical motion does not show much change in intensity variance. Between 25°E and 30°E, there is downward vertical motion that brings in drier air from the upper atmosphere acting as a wall between the Saharan and Arabian high.

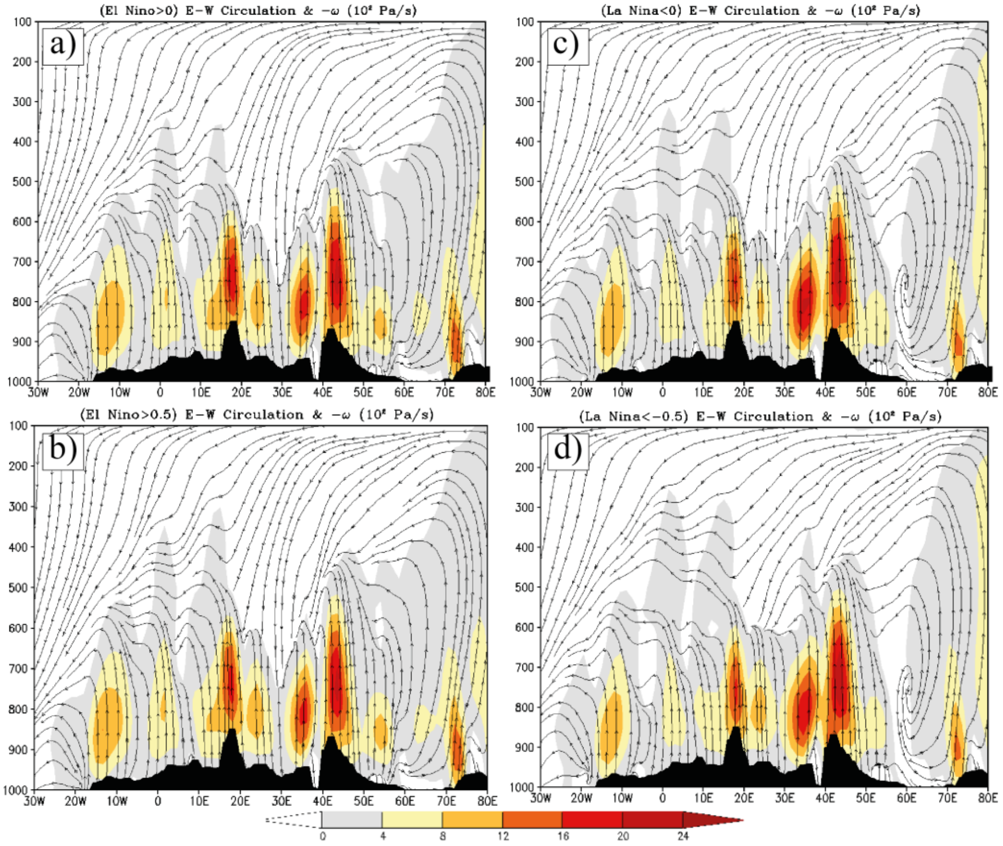

Figure 3.9. Composites of zonal wind and -ω (10^2 Pa s^{-1}) using the MEI for ENSO: (a) MEI > 0 (all positive years), (b) MEI > 0.5 (ENSO years), (c) MEI < 0 (all negative years), and (d) MEI < -0.5 (Non-ENSO years).

During negative ENSO years the east-west circulation cell is present. In contrast to the positive ENSO years during which the tropical easterly jet and low-level westerlies are weaker, the negative ENSO years induces stronger jets which will enhance the zonal components of the east-west circulation. The presence of this cell indicates that the divergence field is strong, which contribute to intensity of the subtropical high pressure systems, especially the Arabian high. With the enhancement of the Arabian high, the pressure gradient will increase the intensity of the LWM_E. The vertical motions over East Africa and into the Arabian Peninsula can be seen with a slight increase in intensity, which is due to the enhancement of the thermal low heating during negative ENSO years.

3.4 Summary

At 600 mb during August (1979-2010) there exist the Saharan and Arabian highs, African easterly jet (AEJ) with two embedded local wind maxima in West and East Africa, and easterly waves over Arabia and Africa easterly waves (AEWs) over Africa. The variability of these synoptic systems is examined. The highest variability occurs over Central Africa, Eastern Africa, and the Arabian Peninsula. For all synoptic systems present, positive (negative) ENSO years will decrease (increase) intensity. For East Africa, the Arabian high's intensity will either increase or decrease the intensity of LWM_E. The LWM_E will help maintain the propagation of easterly waves, especially during extreme Non-ENSO years where the westerly jet reaches into the mid-troposphere and enhance easterly wave intensity. For the AEJ, the zonal gradient is weaker during ENSO years compared to that during Non-ENSO years. This zonal gradient is important in modulating the easterly wave intensity, especially over the Arabian Peninsula. When a strong zonal gradient is present over the Arabian Peninsula, it can help maintain easterly wave propagation.

The higher variance in East African and the Arabian Peninsula is explained by the east-west vertical circulation cell. The presence of this east-west circulation cell provides an indicator to the weakening (strengthening) or the Arabian high during positive (negative) ENSO years. The weak variability of the Saharan high and LWM_W is still not fully understood. Further research can be done for other months and years to see when the Saharan high and LWM_W has the highest variability.

CHAPTER 4

Formation Mechanism of an African Easterly Wave and Mesoscale Convective System over East Africa and Arabian Peninsula: A Numerical Case Study

4.1 Statement of Problem

For this study, we will concentrate on the origin of a coupled *AEW-MCS in August of 2004* (denoted as A04, hereafter) while taking a similar approach that was used to explain vorticity generation in Lin et al. (2013). A04's MCS/convective clusters and A04's AEW/vorticity perturbation will be examined to understand the mechanisms that generate these systems.

4.2 Data and Experiment Design

In order to investigate the formation mechanism of an AEW-MCS system, we need to find the origins of the pre-AEW vorticity maximum and pre-MCS convective cloud clusters, their merging, and the propagation of the merged system. For A04, they are identified by analyzing the data from a collection of datasets. For the analysis of convective cloud clusters, observational globally gridded satellite (GridSat) data from the National Climatic Data Center (NCDC) with an 8 km spatial resolution and 180 minute temporal resolution (Knapp et al., 2011) will be used. The GridSat data serves as reliable observations for cloud clusters and will be compared with the European Centre Medium-Range Weather Forecast Intermediate (ERA-I) dataset at 0.75° x 0.75° globally (Dee et al. 2011) every 6 hours. Using the ERA-I data, analysis will be performed to track both AEWs and convective cloud clusters, and investigate their regions of geneses. The National Oceanic and Atmospheric Administration Climate Prediction Center's Famine Early Warning System (NOAA CPC FEWS) is also used to show daily precipitation associated with A04. The NOAA CPC FEWS data will provide information on that produces rainfall and can be compared with the GridSat and ERA-I datasets to help track A04's convective cloud clusters.

Once a case study is verified from observational analysis, the Weather Research and Forecasting (WRF) model version 3.3.1 will be used to simulate the phenomena. The WRF model is a numerical weather prediction (NWP) and atmospheric simulation system designed for both research and operational applications (Skamarock 2008). The Advance Weather Research (ARW) version of the WRF model is a compressible, three-dimensional, nonhydrostatic model using terrain-following coordinates. The governing equations of ARW are approximated numerically in flux-form with conserved mass and dry entropy. In this study, the Runge-Kutta third-order time and fifth and third order advection schemes were chosen for the horizontal and vertical integrations, respectively. An open (radiative) lateral boundary condition was used in the north-south direction, a free-slip condition was used for the lower boundary condition, and a open lateral boundary condition was used in the east-west direction.

Figure 4.1 illustrates the domain used in WRF to simulate A04. The 24 km outer domain consist of 350 x 180 grid points, 38 vertical levels, and 120 second time steps. The 8 km inner nested domain consists of 652 x 352 grid points, 38 vertical levels, and 40 time intervals. The physics options for both domains include: Goddard microphysics (Tao et al. 1989), RRTM longwave radiation (Mlawer et al. 1997), Duhdia shortwave radiation (Duhdia 1989), Mellor-Yamada-Janjic PBL physics (Janjic 1994), and Betts-Miller-Janjic cumulus parameterization (Janjic 1994).

4.3 RESULTS

4.3.1 Analysis from Observations and ERA-I Data

4.3.1.1 Tracking the Convection of A04. A04 was identified by analyzing Hovmoller diagrams from Gridsat brightness temperature and comparing it with ERA-I cloud cover and relative vorticity. The idea of this comparison was to identify regions of intense easterly waves that originated from the Arabian Peninsula (50°E) and propagated into East Africa. Figure 4.2 illustrates A04's convective cloud cluster that was formed on August 9, 2004 at 06Z [8/9/06Z for simplicity]. The Gridsat and ERA-I's cloud cover compares well enough to proceed with the case study of A04.

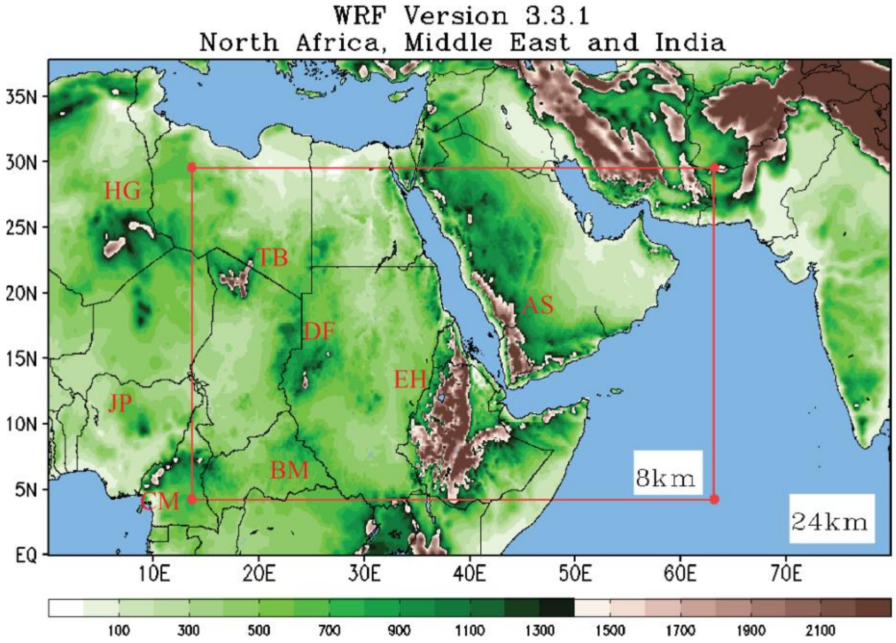

Figure 4.1. Geography for Africa (north of 0°) and southern Arabia Peninsula used for WRF simulations. Labels indicate major geographic features: *AS* - Asir Mountains, *BM* - Bongo Massif, *CM* - Cameron Highlands, *DF* - Darfur Mountains, *EH* - Ethiopian Highlands, *HG* - Hoggar Mountains, *JP* - Jos Plateau, and *TB* - Tibesti Mountains. The outer domain of the simulation is 24 km and the inner domain (red lines) is 8 km resolution.

In Figure 4.2a, the associated convective cloud clusters for A04 can be seen in both Gridsat and ERA-I data at 8/9/06Z over the southern Arabian Peninsula. The convective system propagates over the Asir Mountains at 8/9/18Z and the Ethiopian Highlands at 8/10/06Z where orographic effects are able to enhance the convection. At 8/10/06Z, there is a noticeable convective system over the Ethiopian Highlands. The convective system begins to weaken in the Gridsat at 8/11/06Z, but remains intense in the ERA-I data. Figure 4.2b at 8/11/18Z, the convective cloud clusters propagate away from the Ethiopian Highlands crossing Sudan at 8/12/06Z to 8/12/18Z. At 8/13/06Z, the Gridsat data shows that the convective system has entered a dissipation phase and another convective system forms over the Darfur Mountains at 8/13/18Z. The ERA-I data set does not show dissipation of convection at 8/13/06Z, but did resolve the convective system at 8/13/18Z.

Overall, the ERA-I data compared well with convection from Gridsat, which showed the propagation of A04's convective cloud clusters. Maintenance of convection based on satellite can be attributed to orographic effects from the Asir Mountains, Ethiopian Highlands, and Darfur Mountains, especially during diurnal cycles.

To further strengthen the confidence of A04 from the ERA-I data being a realistic feature, the NOAA CPC FEWS daily precipitation is plotted with ERA-I data 600 mb geopotential heights (Figure 4.3.). On the 8th and 9th of August over the southern Arabian Peninsula, an inverted trough can be seen with little accumulated precipitation associated with it. On August 10, the trough is over the Ethiopian Highlands where precipitation accumulation is increasing. There is a large daily accumulated precipitation flux on August 11 as the trough begins to strengthen. The trough continues to mature on August 12, but the accumulated precipitation decreases. This is consistent with the Gridsat data showing a weak convective system crossing Sudan at 8/12/06Z and 8/12/18Z in Figure 4.2b. By August 13, closed contours of geopotential heights at 600 mb located at (7°N, 19°E) indicate that a mature easterly wave is organizing on the lee side of the Darfur Mountains. It is noteworthy to see during the daily averages of geopotential height that a subtropical high (Arabian High) over the Arabian Peninsula is present. The pressure increases per day for the Arabian in which it will also increase easterly flow on the southern rim of the subtropical anticyclonic zone over southern Arabia and Easter Africa.

4.3.1.2 Relative Vorticity Analysis Using ERA-I Data. In section 4.3.1.1, A04's convective cloud clusters are revealed in the Gridsat and ERA-I total cloud cover data sets. Difficulty of tracing clouds clusters is due to the diurnal variation of cloud clusters. When the convective cloud cluster is weak, its cloud tops are not as cold according to brightness temperature. This suggests a weak phase for the convective cloud clusters, but the associated vorticity may still be present for easier tracking. Figure 4.4 is the 600 mb relative vorticity field from the ERA-I data. The band of positive relative vorticity between 5°N and 15°N is the preferred region of easterly wave propagation. Starting on 8/9/06Z at (14°N, 47°E), there is a strong local maximum of positive vorticity over the southern Arabian Mountains, but the convection is weak according to the GridSat and ERA-I analyses at the same time. This vorticity maximum propagates into the East Africa at 8/10/06Z where it is enhanced by the orographic effects from the Asir Mountains and Ethiopian Highlands. As the vorticity perturbation continues to propagate away from the Ethiopian Highlands at 8/10/18Z, it begins to strengthen and mature.

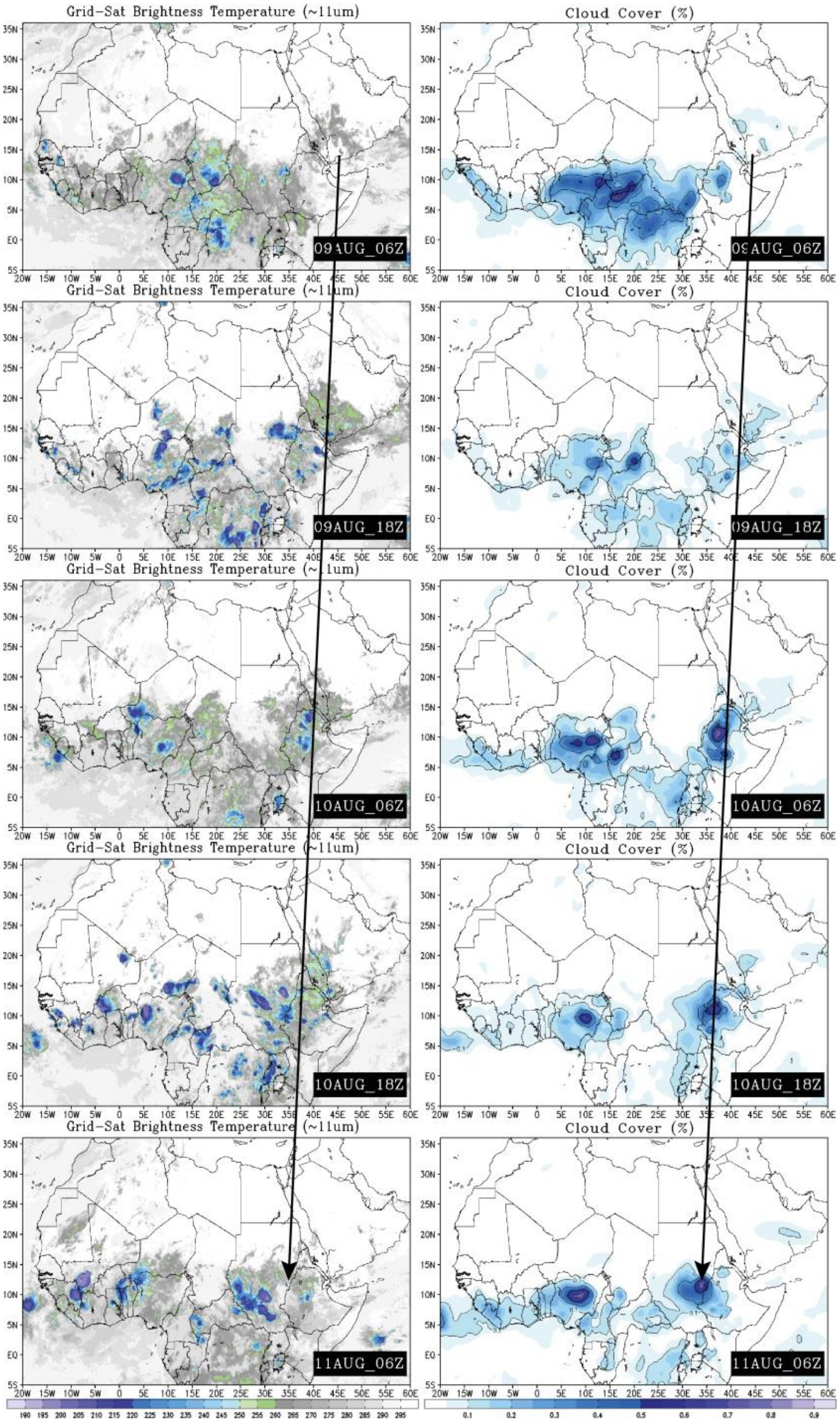

Figure 4.2a. Gridsat (left column) brightness temperature versus ERA-I (right column) total cloud cover (%). Black line denotes track of case study A04 between 8/9/06Z to 8/11/06Z every 12h.

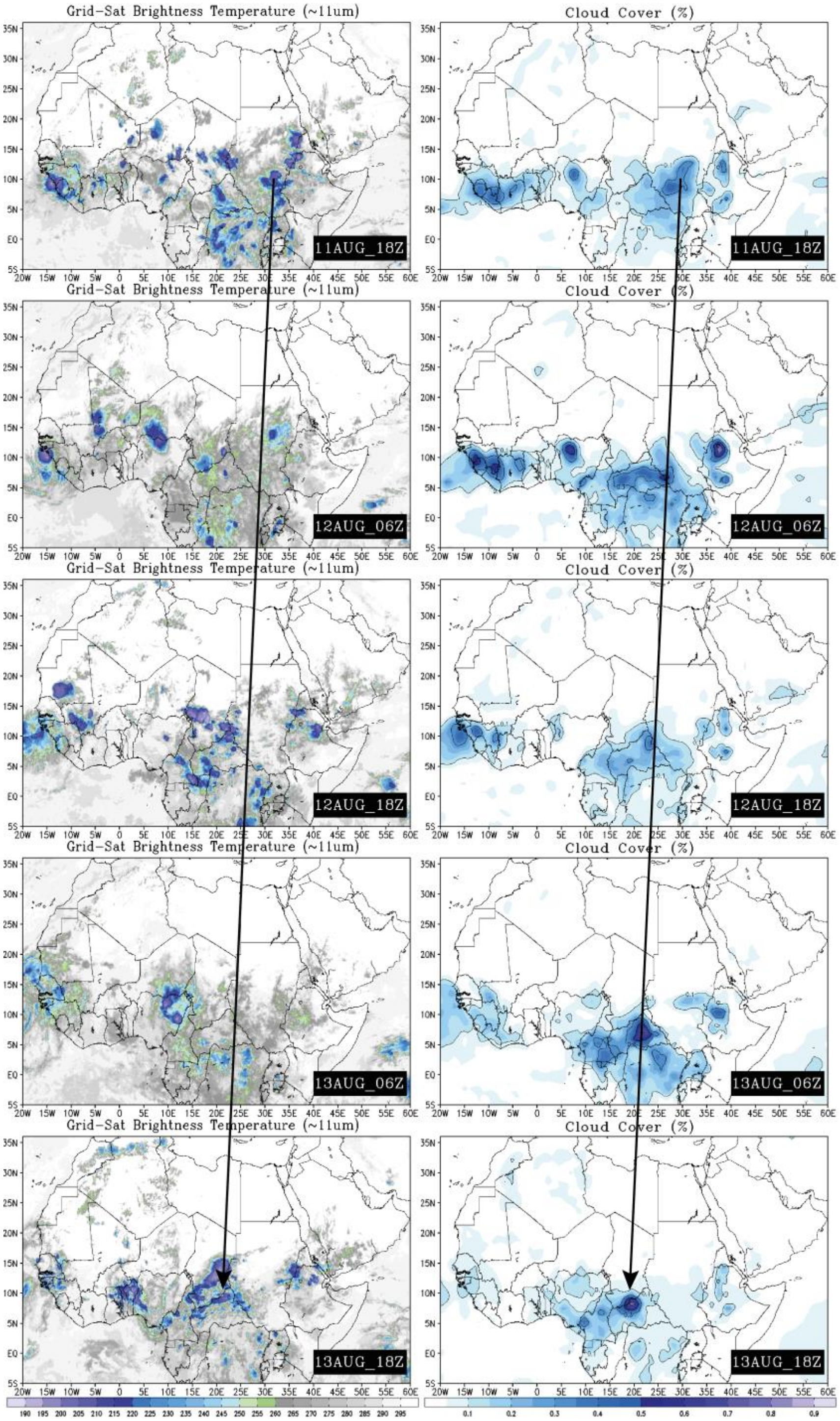

Figure 4.2b. Gridsat (left column) brightness temperature versus ERA-I (right column) total cloud cover (%). Black line denotes track of case study A04 between 8/11/18Z to 8/13/18Z every 12h.

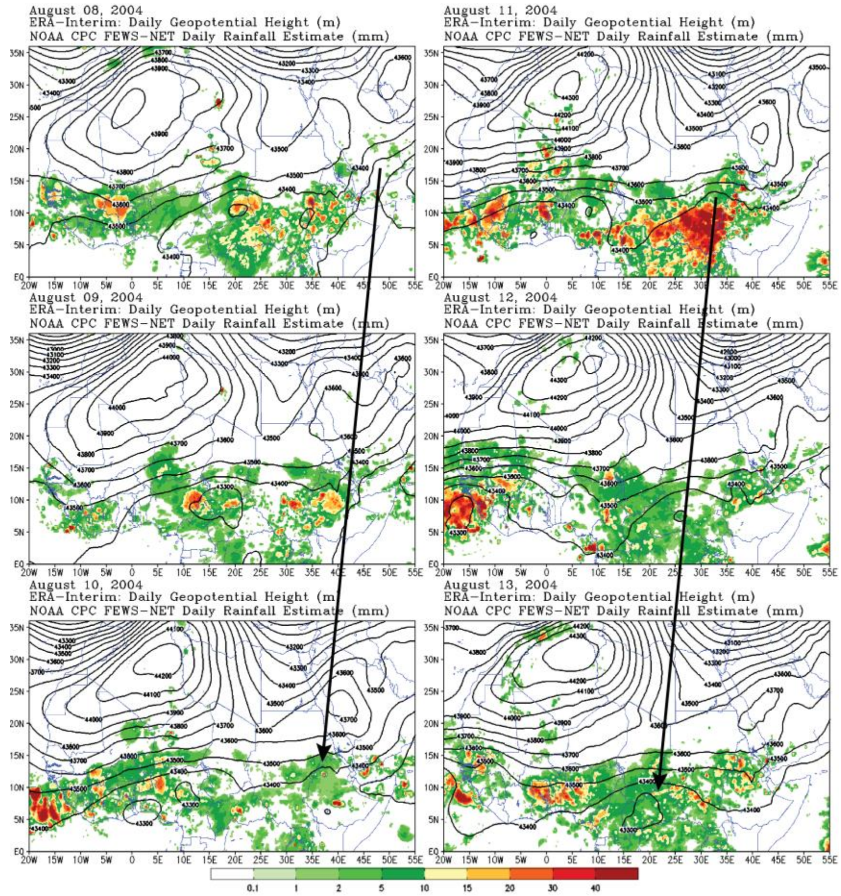

Figure 4.3. NOAA CPC FEWS daily precipitation (mm) shaded and ERA-I 600 mb daily geopotential heights (m) in black contours between August 8th and August 13th. Black line denotes the location of A04.

We will use the vorticity budget to explain the generation of A04's pre-AEW vorticity perturbation over the Arabian Peninsula. The vorticity equation in the isobaric coordinates may be written as (Bluestein 1992):

$$\frac{\partial \zeta}{\partial t} = -\boldsymbol{V} \bullet \nabla\zeta - \omega\frac{\partial \zeta}{\partial p} - v\beta - (\zeta + f)\nabla \bullet \boldsymbol{V} - \hat{k} \bullet \nabla\omega \times \frac{\partial \boldsymbol{V}}{\partial p} + \hat{k} \bullet \nabla \times Fr \qquad (1)$$

The above equation examines the local rate of change of vorticity from a mechanical perspective. After analysis of the relative vorticity field, earliest detection of A04's pre-AEW vorticity perturbation was at 8/9/00Z. Magnitudes for local rate of change, horizontal vorticity advection, vertical advection, and divergence are at an order of 10^{-10} s^{-2}. The local rate of change of vorticity shows the evolution of vorticity between 8/8/18Z to 8/9/06Z (Figure 4.5a). Applying the central differencing in time to approximate the local rate of change yields the detection time of A04's pre-AEW vorticity perturbation located at (15°N, 47°E). The positive horizontal vorticity advection has the highest magnitude between all the terms (Figure 4.5b). Easterly zonal wind flow will aid advection of relative vorticity, therefore adding to the intensity of the magnitude of horizontal advection. The positive vorticity advection of A04's pre-AEW vorticity perturbation is located at (15°N, 48°E) at 8/9/00Z. The presence of the Asir Mountains induces vertical advection of vorticity that is generated from the diurnal cycle (Figure 4.5c). The source of vertical motion is also associated with convection generated from ITCZ heating.

Note that preexisting relative vorticity (ζ) is included in each term of Eq. 1, except the divergence term $-f\nabla \bullet \boldsymbol{V}$ and the friction term. Since f is dependent on the Earth's rotation, then convergence and f, i.e. stretching of planetary vorticity may generate vorticity. Figure 4.5d at 8/9/00Z, shows A04's pre-AEW vorticity perturbation being generated over the Arabian Peninsula located at (15°N, 48°E). Comparisons are done (not shown) between the magnitudes of $f\nabla \bullet \boldsymbol{V}$ and $\zeta\nabla \bullet \boldsymbol{V}$ and it was found that $f\nabla \bullet \boldsymbol{V}$ had the higher magnitude. In the beginning, there was no vorticity present, but then the $f\nabla \bullet \boldsymbol{V}$ term helps generate relative vorticity by planetary vorticity stretching. Later, the $\zeta\nabla \bullet \boldsymbol{V}$ term comes into play to strengthen the vorticity generation once the relative vorticity has been generated by the planetary vorticity stretching. The sources of the vorticity perturbations were attributed to convergence of southeasterly Shamal winds, which is associated with the Arabian high and the northwesterly Somali jet winds, that is associated with the Indian Ocean high (Lin et al. 2013). These interaction increases vorticity generation until the vorticity is advected by the mean easterly wind flow of the AEJ.

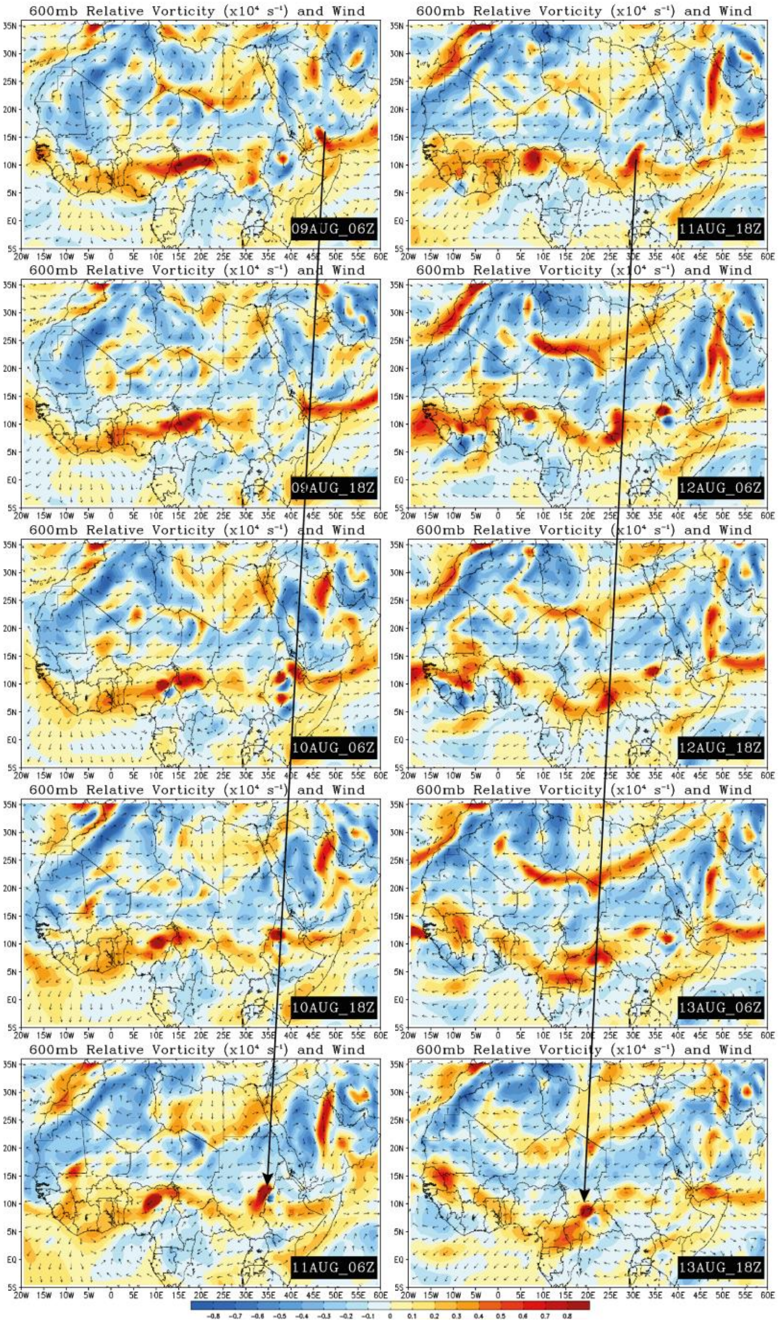

Figure 4.4. ERA-I 600 mb relative vorticity (s^{-1}) and wind vectors between 8/9/06Z to 8/13/18Z every 12 hours. Red (blue) shade is for positive (negative) vorticity. Black line represents the track of A04.

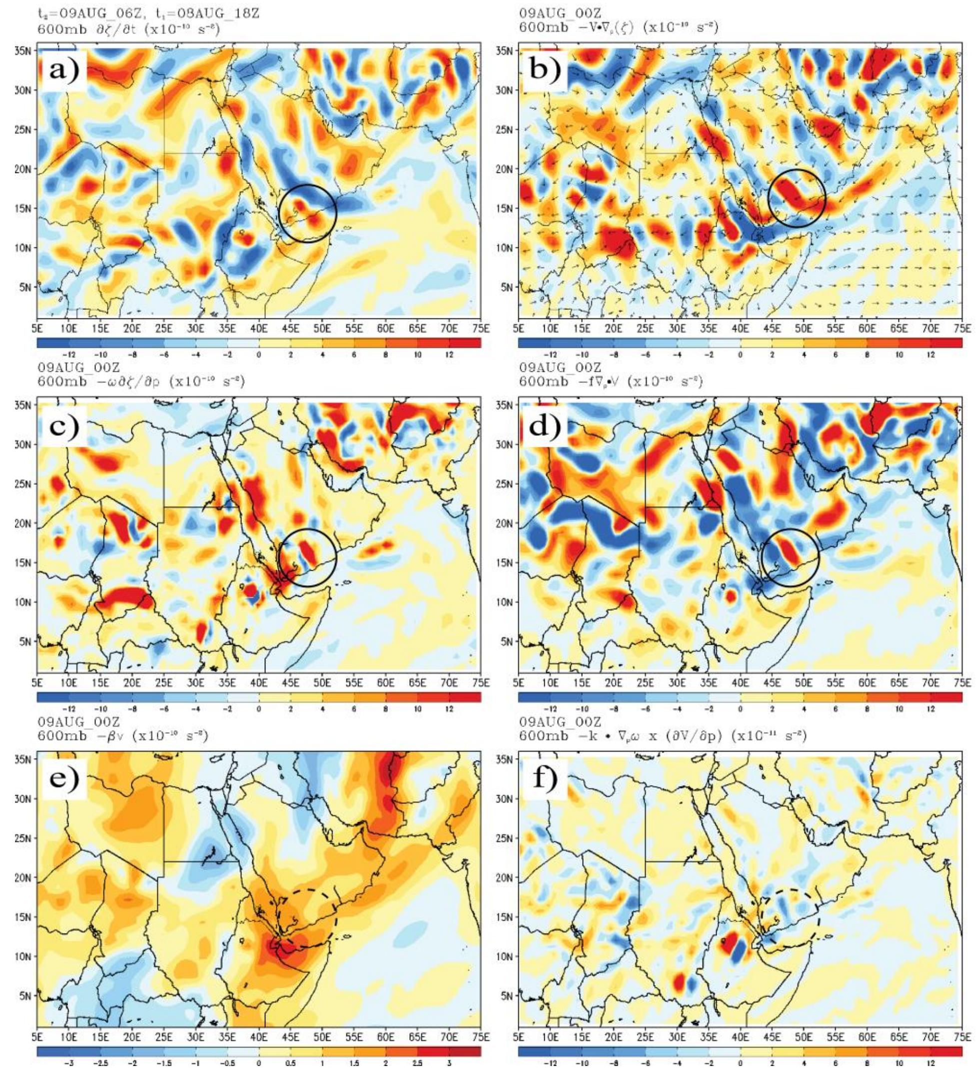

Figure 4.5. ERA-I 600 mb vorticity budget analysis of (a) local rate of change (x10^{-10} s^{-2}) from t_1 = 8/8/18Z to t_2 = 8/9/06Z and, (b) vorticity advection (x10^{-10} s^{-2}), (c) vertical vorticity advection (x10^{-10} s^{-2}), (d) divergence (x10^{-10} s^{-2}), (e) beta effect (x10^{-10} s^{-2}), and (f) tilting (x10^{-11} s^{-2}). Terms in (b) – (f) are calculated at 8/9/00Z. The black circles denote where A04 is located.

The beta effect (Figure 4.5e) shows the drifting planetary vorticity advection. The meridional gradient of planetary vorticity is high over the Arabian Peninsula in comparison to East Africa because of the southerly meridional winds over the Arabian Peninsula are strong. The southerly winds are associated with the Arabian high and Shamal winds. Even though the magnitudes of the beta term is the same order of $-\boldsymbol{V} \bullet \nabla\zeta, -\omega\frac{\partial\zeta}{\partial p}, and - f\nabla \bullet \boldsymbol{V}$; the values are smaller than the respective terms. The titling term (Figure 4.5f) is at an order of 10^{-11} s^{-2} and therefore is negligible in comparisons to the higher ordered terms.

The relative vorticity field and budget analysis of A04's pre-AEW vorticity perturbation using the ERA-I data provides realistic details about wave genesis over the Arabian Peninsula. It was found that A04's pre-AEW vorticity perturbation was generated around 8/9/00Z and was a mature AEW at 8/13/18Z. This will be essential for setting up a time interval to simulate A04 using the WRF model.

4.3.2 WRF Results

4.3.2.1 Model Performance and Comparison to ERA-I Data. The WRF simulation uses the ERA-I data at 9/8/00Z to initialize and is ran until 8/15/00Z, outputted every 3 hours. A series of experiments are performed to identify possible physics parameterization combinations that would reproduce A04. Figure 4.6 illustrates the various combinations using daily rainfall totals and 600 mb geopotential height with the corresponding combinations in Table 3.

The parameterization combinations that over predicted precipitation came from WSM 6 Class, Thompson, Kain-Fritsch, and Grell 3D ensemble (Figure 4.6a-d). The precipitation is a result from convection being over intensified or producing unrealistic convective processes. These results does not compare well with Figure 4.3. The Goddard and Lin schemes (Figure 4.6e-h) performed better in terms of precipitation reliability and cumulus schemes were narrowed down to Betts-Miller-Janic (Figure 4.6g and h). After close inspection and comparison between physics parameterization combinations, the Goddard microphysics and Betts-Miller-Janic cumulus parameterization are used as the control simulation for this case study.

The calculated relative vorticity magnitudes are stronger in the WRF simulation in comparison with the ERA-I analyzed field. This is due to increased resolution of 8 km in the simulation. In Figures 4.7, the WRF simulated 600 mb horizontal wind (Figures 4.7a and b) can be compared with the ERA-I data (Figure 4.7c and d) to show the intensity difference between the model and reanalysis data. The x and y components of relative vorticity are $\partial u/\partial y$ and $\partial v/\partial x$. An increase of intensity from either component will intensify the overall relative vorticity. The most noticeable difference of intensity comes from the simulated zonal wind (Figure 4.7a) versus the ERA-I zonal wind field (Figure 4.7c). The easterly wind between 9°N and 21°N shows the existence of the AEJ. Spinks et al. (2014) investigated the AEJ over East Africa and found a local wind maximum embedded within the AEJ centered at (14°N, 35°E). This local wind maximum in East Africa (LMW_E) is also present in the simulation and ERA-I analyzed field, but the intensity is significantly different. For the WRF simulated and ERA-I data, the intensity of the LMW_E is 12 to 14 $m\ s^{-1}$ and 10 to 12 $m\ s^{-1}$, respectively. Westerly wind has a stronger presence over East Africa centered at (6°N, 20°E) in the simulation versus that in the ERA-I field. The magnitude of the easterly wind is stronger over the Arabian Peninsula as well.

The reason for the stronger zonal wind speed in the simulation versus the ERA-I data, is due to stronger geopotential height. The Arabian high can be seen in the WRF simulated and the ERA-I analyzed fields, which are centered at (21°N, 37°E) and (21°N, 43°E), respectively (Figures 4.7a and c). The geopotential heights are larger in the WRF simulation for the Arabian high by about 1000 m and the size of the anticyclone is broader. The increased geopotential heights, induces a stronger positive meridional geopotential gradient, which then increases the easterly zonal wind speed that produces stronger relative vorticity over East Africa and the Arabian Peninsula.

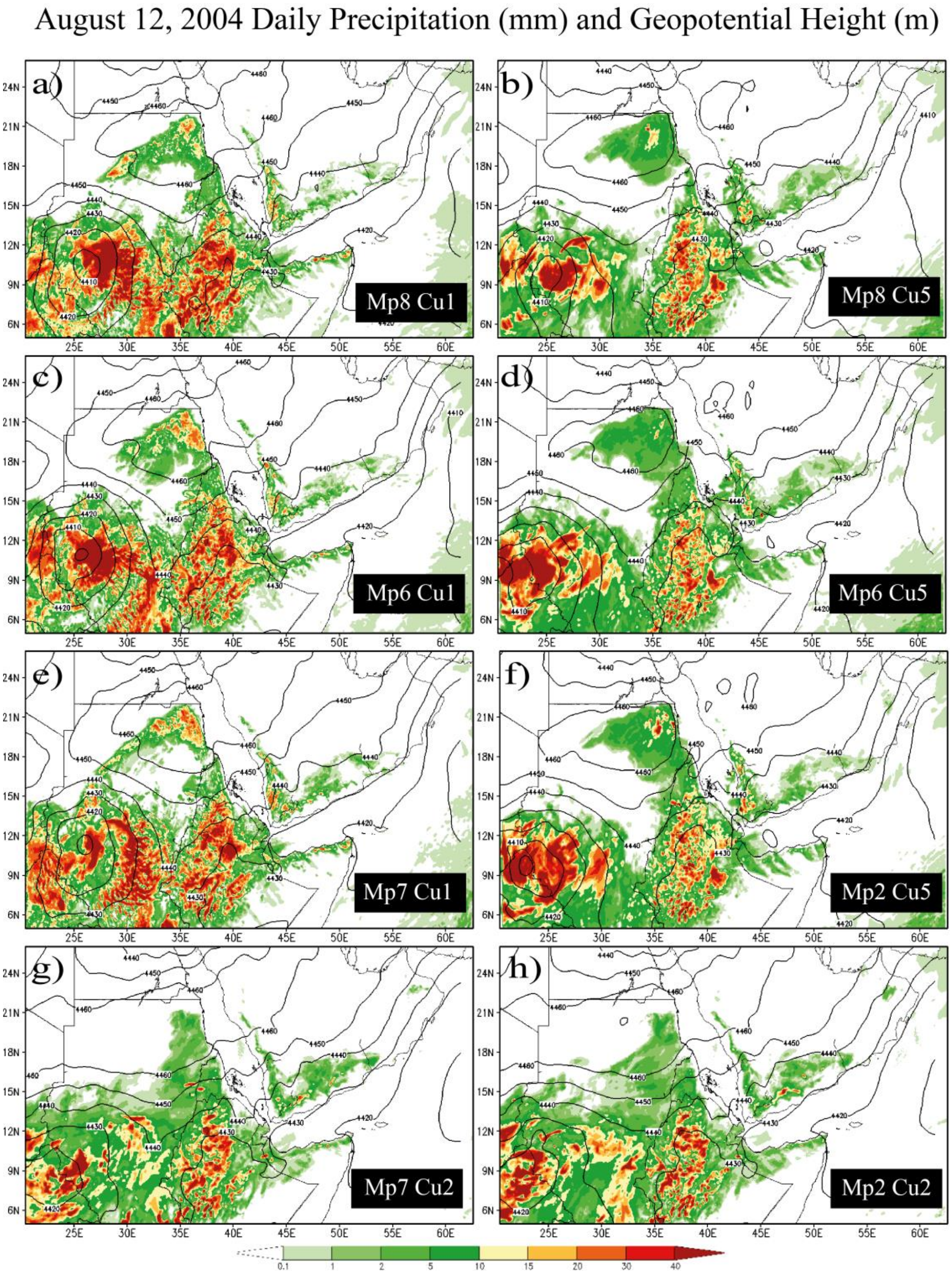

Figure 4.6. WRF simulated daily precipitation (mm) shaded and 600 mb geopotential height (m) in black contours for multiple physics schemes. The corresponding combination of physic schemes can be seen in Table 3.

Table 3

Physics combinations used to test the performance of the WRF model. Experiment G is used for the main simulation.

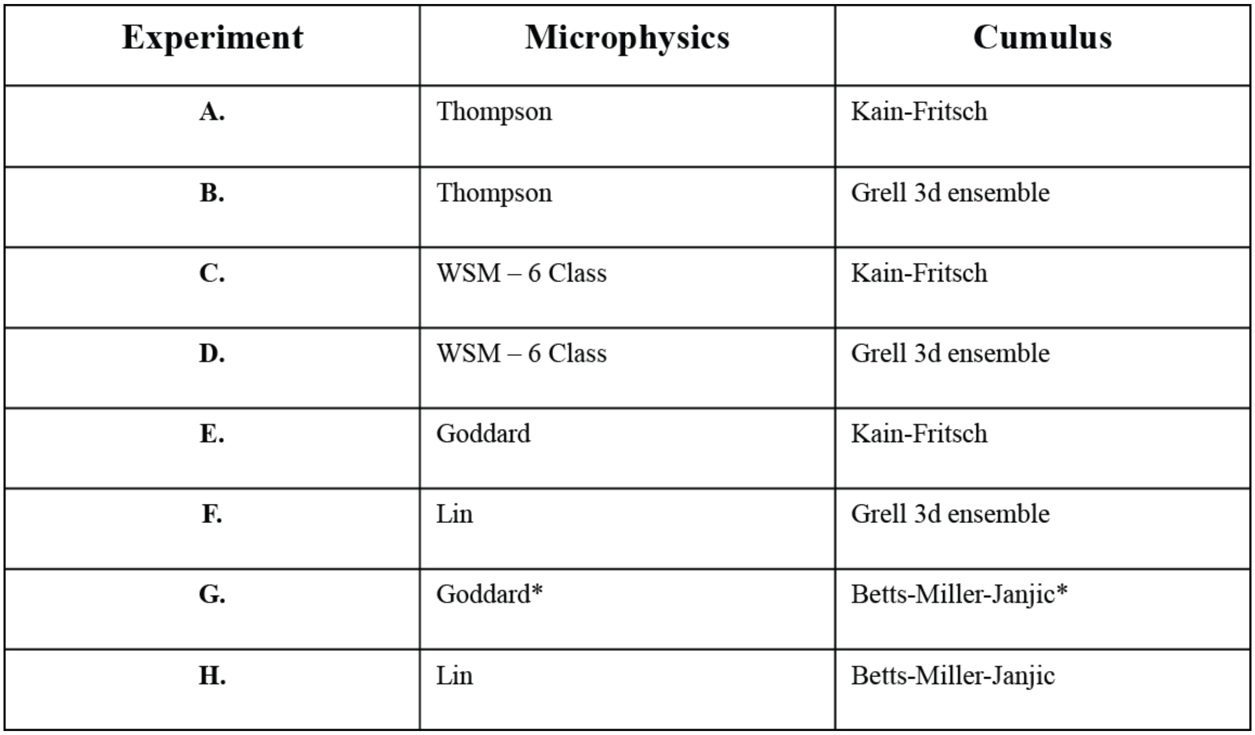

Experiment	**Microphysics**	**Cumulus**
A.	Thompson	Kain-Fritsch
B.	Thompson	Grell 3d ensemble
C.	WSM – 6 Class	Kain-Fritsch
D.	WSM – 6 Class	Grell 3d ensemble
E.	Goddard	Kain-Fritsch
F.	Lin	Grell 3d ensemble
G.	Goddard*	Betts-Miller-Janjic*
H.	Lin	Betts-Miller-Janjic

Comparing Figure 4.6 to Figure 4.3, it can be seen how the model performs against the NOAA CPC FEWS daily precipitation and ERA-I geopotential height. Precipitation is used as a diagnostic variable to determine the best choice of physical parameterization combinations.

Comparison of meridional wind between the WRF simulated and ERA-I analyzed fields (Figure 4.7b and d), shows minor difference in wind speed. This means that the relative vorticity increase mainly comes from the zonal wind component. The northerly winds over the Arabian Peninsula, which is centered at (20° N, 43° E), is associated with the Arabian high. The northerly jet located in the southeast Arabian Peninsula is resulted from the northwest-southeast gradient of the converging Arabian subtropical high and Indian Ocean high.

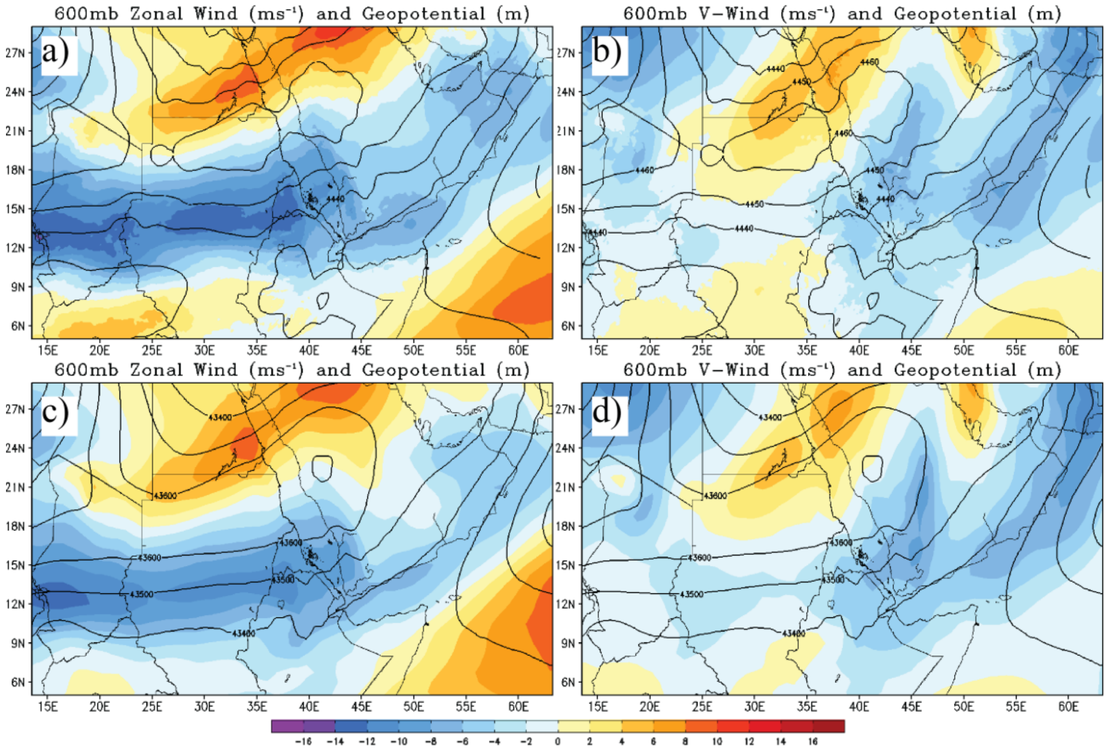

Figure 4.7. The 6-day average between 8/9/00Z and 8/15/00Z of WRF simulated 600 mb (a) zonal wind and (b) meridional wind speed (shaded) superimposed with geopotential height (m) (contours). Panels (c) and (d) are the same as (a) and (b) except for ERA-I analyzed fields.

The relative vorticity magnitudes are higher in the WRF simulation versus the ERA-I analyzed fields. Since the WRF simulation also is able to resolve more detailed vorticity processes in vorticity generation, it provides us more detailed information, which were absent from the ERA-I data. The next section will discuss the WRF simulated vorticity fields, and propose three stages of their evolution for the African easterly wave A04.

4.3.2.2 Three Stages of A04: Formation, Merger, and Mature. Vorticity budget analysis at 600 mb from the 24km WRF simulation will reveal genesis mechanisms that will explain the origin of A04's pre-AEW vorticity perturbation. In section 4.3.1.2, budget analysis was performed using the ERA-I. In section 4.3.2.1, it was explained that the calculated relative vorticity in the WRF simulation will have a higher magnitude than the vorticity from the ERA-I data. In Figure 4.8, the vorticity budget from the simulation uses the same variables as Eq. 1 in Figure 4.5 from the ERA-I analyzed field. The origin of A04's pre-AEW vorticity perturbation was traced to 8/9/00Z, so we used central differencing of time for the local rate of change, where t_1 = 8/8/21Z and t_2 = 8/9/03Z. The magnitudes of vorticity show an increase of intensity in comparison to the local rate of change in the ERA-I analyzed field. A04's pre-AEW vorticity perturbation is located at (15°N, 47°E) and the order of the local rate of change is as high at 10^{-10} s^{-2}. The vorticity advection is the largest between all terms (Figure 4.8b). Positive vorticity advection is dominant along the southern Arabian Mountains and is enhanced from orographic effects under the basic easterly wind flow in the mid-troposphere. The increased meridional zonal gradients of the relative vorticity make the major contribution to the increase of vorticity advection. It was shown in Figure 4.7, that the meridional wind component has little increase of magnitude to vorticity, so the meridional vorticity advection component of $-\mathbf{V} \bullet \nabla\zeta$ is smaller than the zonal component. Instead, the meridional component is important for cyclonic vorticity generation from to the interactions of the northerly and southerly winds components converging at (15°N, 48°E).

The relative vorticity generated by the planetary vorticity stretching associated with the cyclonic vorticity convergence may be advected downstream zonally (westward) as well as vertically by upward motion. For A04's pre-AEW vorticity perturbation, the southern Arabian Mountains was the source of vertical motion as induced by the diurnal cycle and easterly wind flow over the mountains. The term $-\omega\frac{\partial\zeta}{\partial p}$ helps advect the relative vorticity generated by the cyclonic vorticity convergence associated with the interaction of Arabian High and Indian Ocean High. This enhancement of relative vorticity by vertical advection may be further strengthened by vorticity stretching associated with the formation of cloud clusters through latent heating.

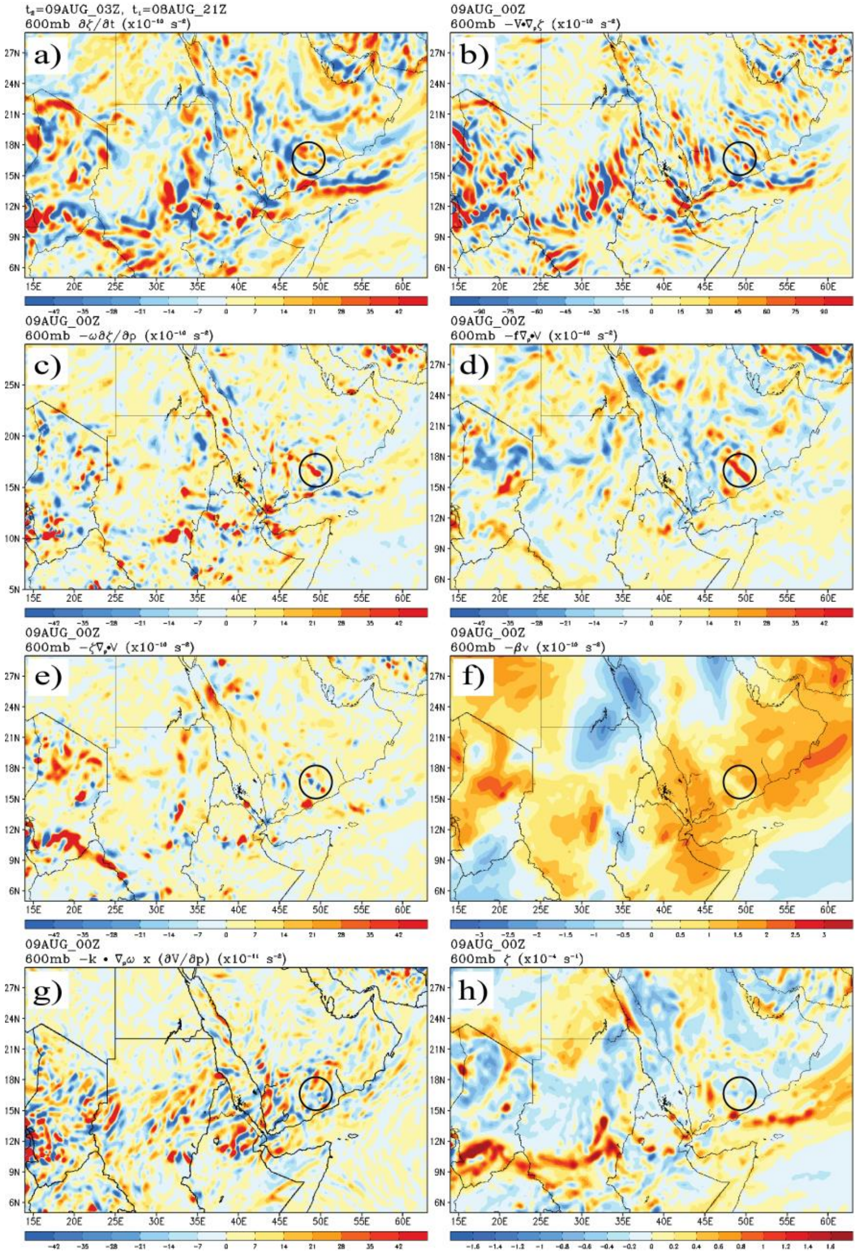

Figure 4.8. Vorticity budget analysis of the 24km WRF simulated 600 mb field: (a) local rate of change (x10^{-10} s^{-2}) from t_1 = 8/8/21Z to t_2 = 8/9/03Z, (b) vorticity advection (x10^{-10} s^{-2}), (c) vertical vorticity advection (x10^{-10} s^{-2}), (d) –*f* and divergence (x10^{-10} s^{-2}), (e) –*ζ* and divergence (x10^{-10} s^{-2}), (f) beta effect (x10^{-10} s^{-2}), (g) tilting (x10^{-11} s^{-2}), and (h) relative vorticity (x10^{-4} s^{-1}). Terms (b) – (h) are calculated at 8/9/00Z. The black circles denote the locations of the African easterly wave A04.

The divergent term $-f\nabla \bullet \boldsymbol{V}$ is the most important factor to explain relative vorticity generation by the stretching of planetary vorticity from the cyclonic convergence of the highs. Once relative vorticity is generated, orographic effects from the Arabian Mountains continues enhancement of vorticity. In Figure 4.8d, A04's pre-AEW vorticity perturbation is located at (15°N, 48°E) with strong convergence over the southern Arabian Mountains. The zeta and convergence term is small because relative vorticity for A04 has not been generated (Figure 4.8e). The magnitudes of the beta (Figure 4.8f) and titling terms (Figure 4.8g) are the smallest and therefore are not significant to the generation of relative vorticity. Comparing the magnitudes, the terms $\frac{\partial \zeta}{\partial t}$, $-\boldsymbol{V} \bullet \nabla\zeta$, and $-f\nabla \bullet \boldsymbol{V}$ are the most significant and clearly shows how A04's pre-AEW vorticity perturbation is generated from convergence, the advection of vorticity, and the local rate of change of vorticity. The diurnal cycle will help induce orographic generated vorticity along with convergence of the Arabian high northerlies and southerlies from the Indian Ocean high. The vorticity advection has the highest order and works complementary with the easterly flow over southern Arabia Peninsula.

Lin et al. (2005) found that there are two modes of the pre-Alberto (2000) MCSs embedded within the AEW structure: a stationary mode and a propagating mode. The stationary mode exists over the Ethiopian Highland on a diurnal basis due to sensible heating over the high terrain. The propagation mode coincides with the propagation and generation of AEWs in the vicinity of the Ethiopian Highlands. In a later study, Lin et al. (2013) found a stationary mode of over the southern Arabian Mountains, which was proposed to be the genesis region for the pre-Debby AEW-MCS precursor. The two stationary modes of vorticity generation over the Ethiopian Highlands and Arabian Mountains influence the genesis of A04's pre-AEW vorticity perturbation.

Figure 4.9a illustrates the formation and evolution phase of A04's associated convective cloud cluster and vorticity from the outgoing long wave radiation (OLR) and relative vorticity field, respectively. There are two distinct areas of orographic generated lee vorticity and convection that contribute to the formation of A04. At 8/9/06Z, the vorticity perturbation and convective cloud cluster at (12°N, 40°E) over the Ethiopian Highlands is a pre-AEW and pre-MCS (denoted as PAM-1). The vorticity perturbation and convective cloud cluster located at (15°N, 47°E) over the southern Arabian Peninsula is PAM-2. The pre-AEW system associated with PAM-2 is generated by cyclonic vorticity convergence from the planetary vorticity stretching and then enhanced by relative vorticity, while the pre-MCS for both PAM-1 and 2 are generated by the mountains through diurnal heating. The generation of convective cloud clusters and vorticity perturbations over the mountains is part of the stationary mode. The biggest difference between the relative vorticity fields of the 8 km WRF simulation and the ERA-I is that the simulation resolves more orographic generated vorticities, especially during the diurnal cycles.

At 8/9/18Z, PAM-1 and PAM-2 are being enhanced by the Ethiopians Highlands and Asir Mountains, respectively. The convective cloud clusters associated with PAM-1 becomes better organized, while PAM-2 is propagating into East Africa by 8/10/06Z. At 8/10/18Z, the two systems are very noticeable by the olr field. PAM-1 is located over South Sudan at (9°N, 30°E) and PAM-2 is located over the Ethiopian Highlands at (14°N, 37°E). After the formation stage of PAM-1 and PAM-2, the systems propagated at the same speeds of 8.5 m s^{-1}.

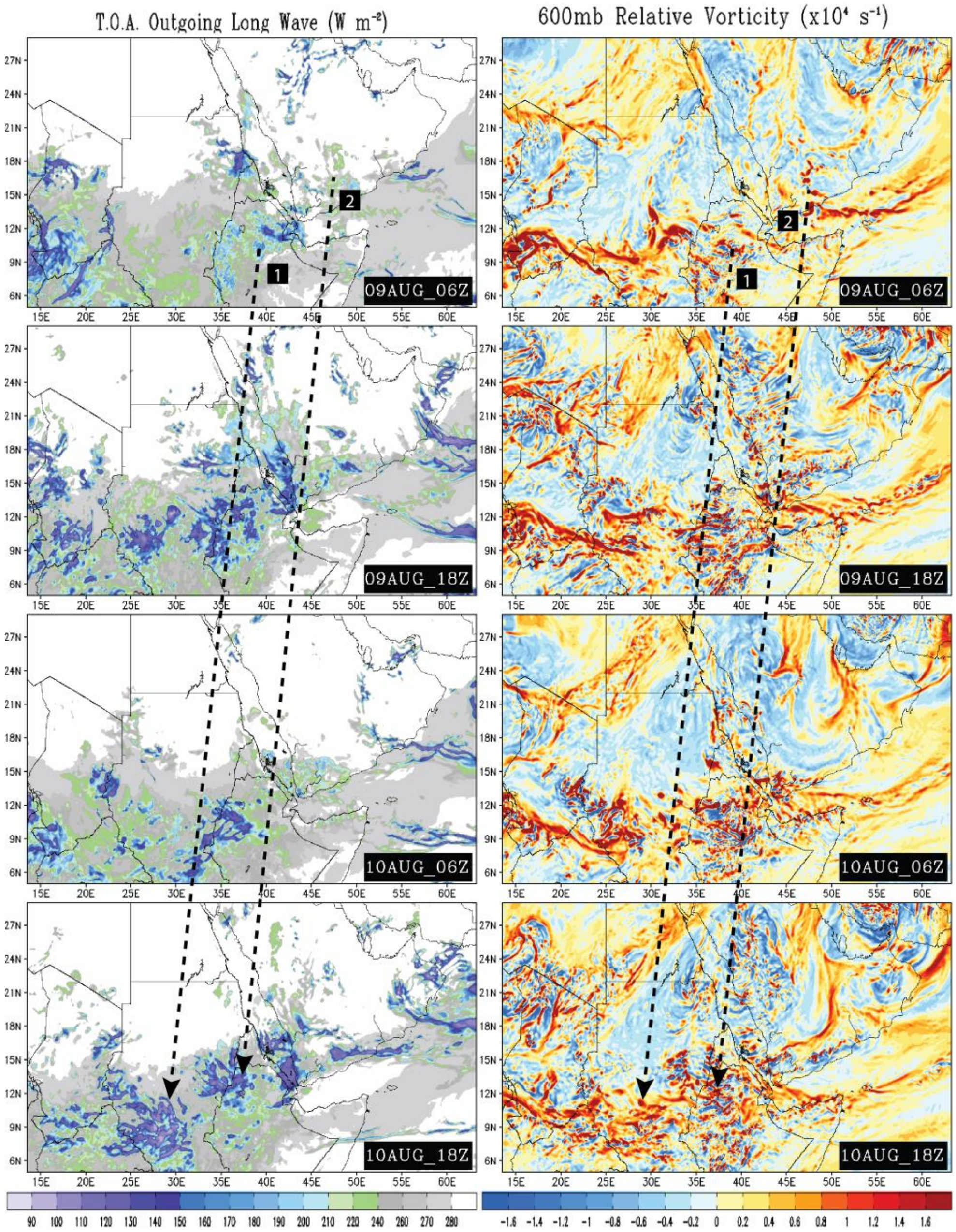

Figure 4.9a. WRF simulated outgoing long wave radiation (OLR; in W s^{-2}) shaded in the left column and 600 mb relative vorticity (10^{-4} s^{-1}) shaded in the right column. Time interval is between 8/9/06Z to 8/10/18Z every 12 h. Line 1 denotes the pre-AEW and pre-MCS (PAM-1) over the Ethiopian Highlands and line 2 denotes the pre-AEW and pre-MCS (PAM-2) over the southern Arabian Peninsula.

The final stage is mature phase (Figure 4.9c). PAM-1 and 2 are now completely merged together and has become a mature AEW-MCS, known as A04. At 8/13/06Z, A04 can be seen on the lee of the Darfur Mountains as a well-organized system. The system propagates off to the west while maintaining as an intense AEW-MCS until it out of the domain at 14/18Z. The propagation speed of the A04 is 8.5 m s^{-1}.

4.3.2.3 Evolution of the AEJ and Embedded East Local Wind Maximum. During A04's evolution across the southern Arabian Peninsula and East Africa, the AEJ played an important role in maintaining the system's intensity and integrity. The AEJ has been long understood to support the growth of AEWs through the barotropic-baroclinc mechanism (Charney and Stern 1962; Burpee 1972; Rennick 1976; Mass 1979; Thorncroft 1995, Grist et al. 2002). In recent studies, it have been proposed that AEWs are triggered by MCS over the Darfur Mountains (Berry and Thorncroft 2005; Mekonnen et al. 2006), the Ethiopian Highlands (Lin et al. 2005), and the southern Arabian/Asir Mountains (Lin et al. 2013). This section attempts to show the evolution of the AEJ in East Africa and Arabian Peninsula and the growth of A04 along the jet. The triggering of A04 from MCSs and convergence was already established in the previous section 4.3.2.2.

As demonstrated in Spinks et al. 2014, the AEJ over northern Africa has an embedded local wind maximum, namely $LWM_{E,}$ in East Africa. The intensity of LWM_E at near (35°E, 15°N) has an averaged zonal wind speed of -9.81 m s^{-1} for the month of August. In particular, the LWM_E is a contributing factor to the maintenance and propagation of easterly waves over southern Arabian Peninsula and East Africa.

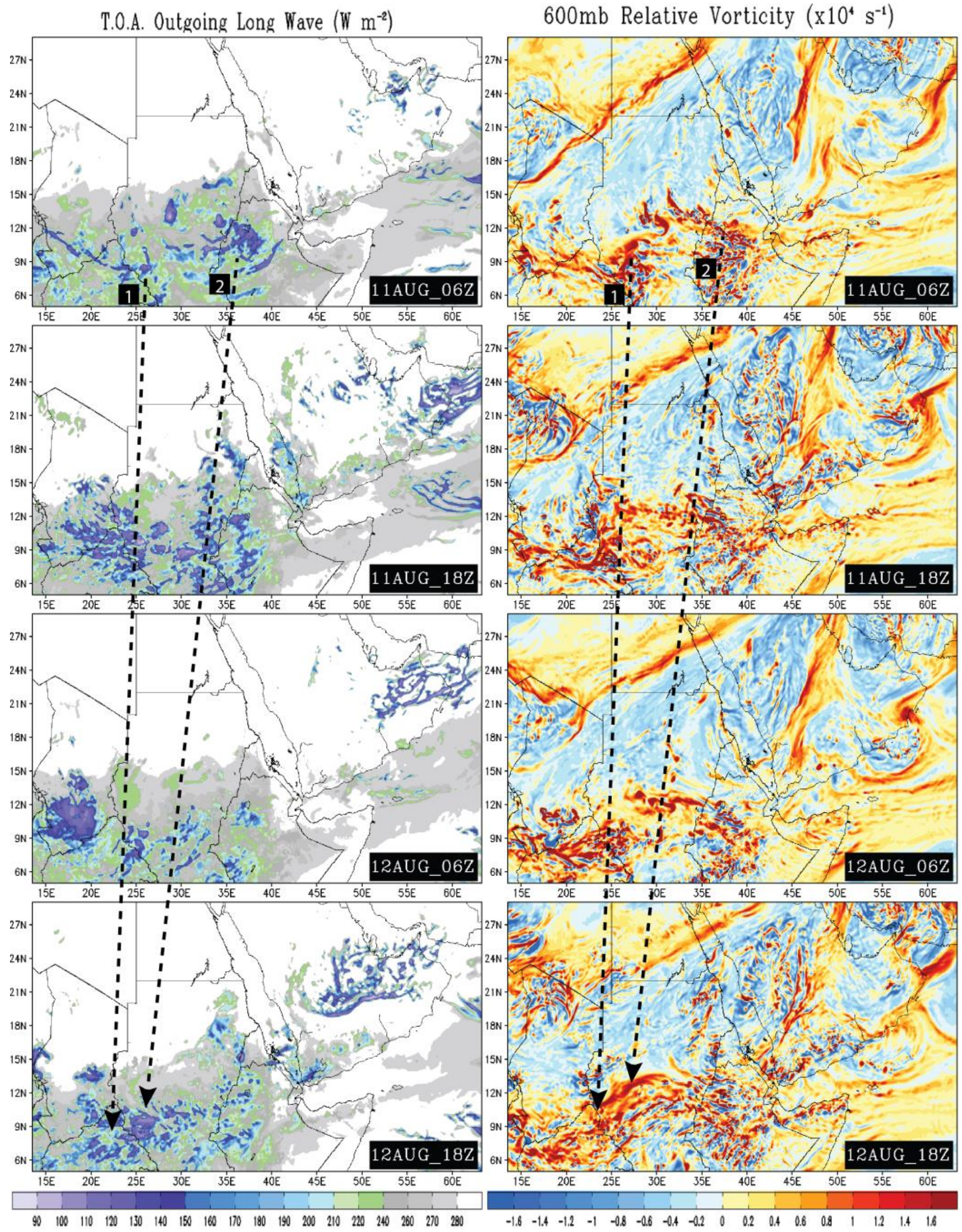

Figure 4.9b. WRF simulated outgoing long wave radiation (OLR; in W s^{-2}) shaded in the left column and 600 mb relative vorticity (10^{-4} s^{-1}) shaded in the right column. Time interval is between 8/11/06Z to 8/12/18Z every 12 h.

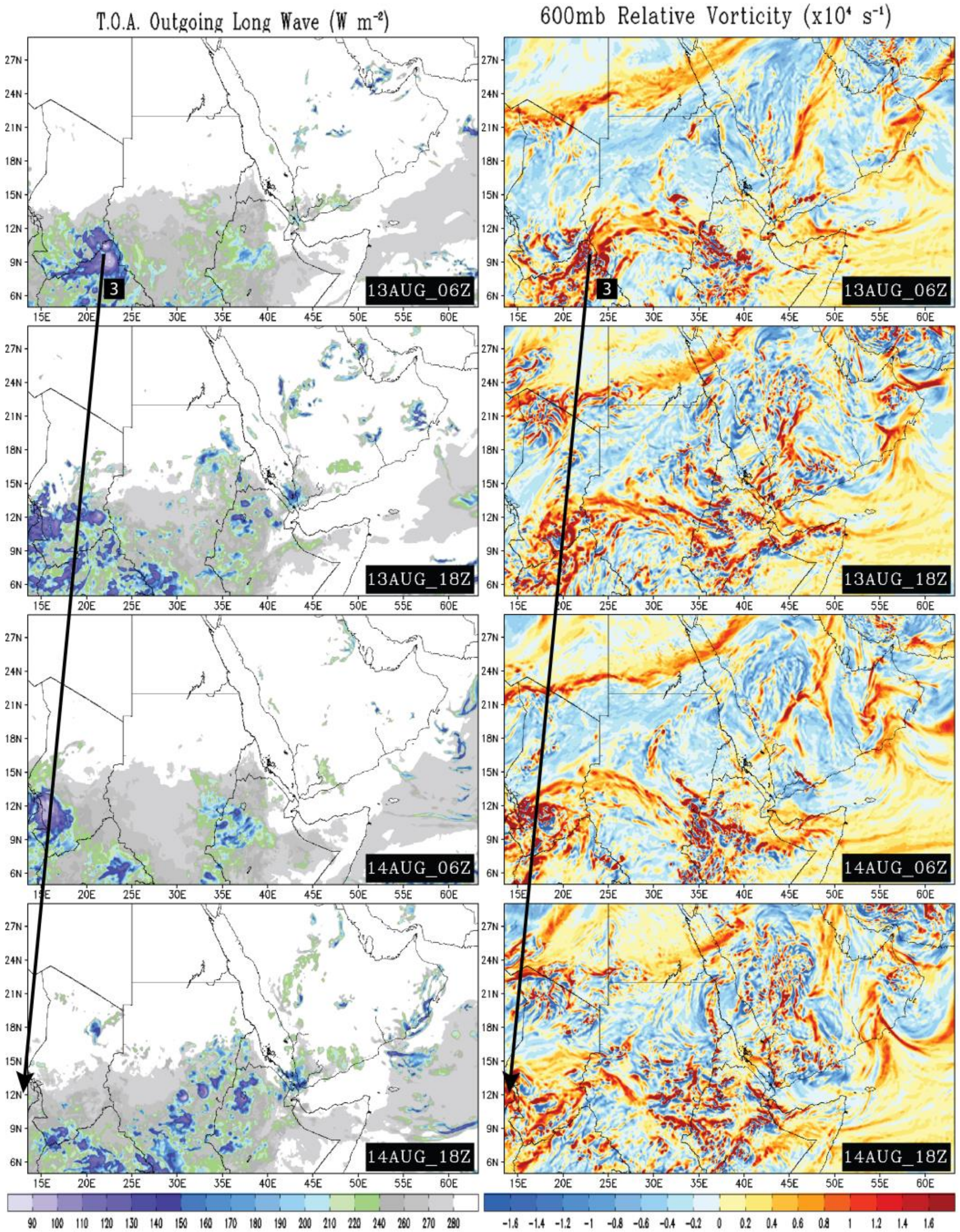

Figure 4.9c: WRF simulated outgoing long wave radiation (OLR, in W s^{-2}) shaded in the left column and 600 mb relative vorticity (10^{-4} s^{-1}) shaded in the right column. Time interval is between 8/13/06Z to 8/14/18Z every 12 h.

By 8/11/06Z, the LWM$_{\text{E}}$ located at (15°N, 35°E) is in a mature phase with velocities greater than 16 m s^{-1} and the Arabian High is centered at (21°N, 35°E). This is also the start of the merging phase of PAM-1 and PAM-2 in section 4.3.2.2. At 8/12/06Z, the LWM$_{\text{E}}$ located at (13°N, 27°E) and the presence of westerly wind centered at (5°N, 25°E) will increase the meridional zonal gradient and enhance easterly wave development, which can be seen at (8°N, 24°E). By 8/13/06Z, the LWM$_{\text{E}}$ is coupled with A04 and is in a mature phase while propagating. As the systems continue to propagate to the west, the LWM$_{\text{E}}$ is separated from the dominate influence of the Arabian high and is intercepted by the Saharan high after crossing 20°E.

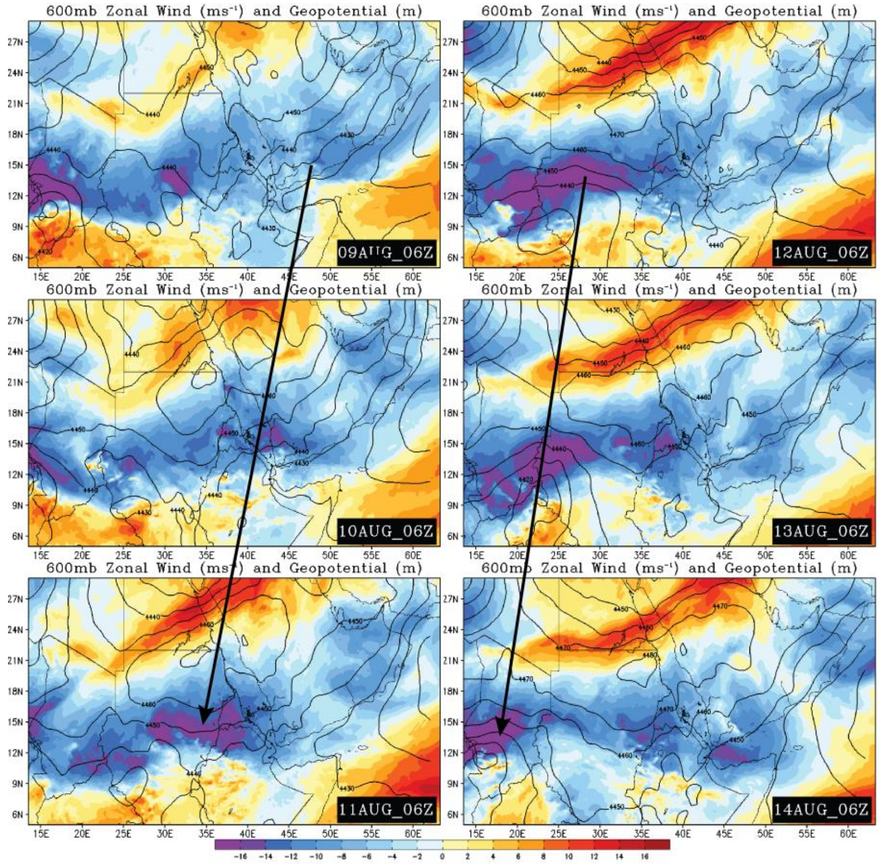

Figure 4.10. WRF simulated 600 mb zonal wind (shaded every 2 m s^{-1}) and geopotential height (m) (contours) from 8/9/06Z and 8/14/06Z for every 24 h. The thick black lines denote the locations of the maximum zonal winds associated with A04.

The LWM_E helps maintain A04 from the maximum easterly wind flow induced from the Arabian high's meridional geopotential gradient. This component is essential for the survival of the pre-AEW vorticity perturbation over the Arabian Peninsula and East Africa. The orographically generated lee vorticities are part of the stationary mode and will need the presence of easterly wind flow in order to propagate away from the mountains. Once split from the mountains, the pre-AEW vorticity perturbations are able to grow under the influence of the LWM_E. The existence of the westerly wind to the south of the easterly wind will also be a contributing factor to vorticity maintenance when the zonal gradient is robust.

4.4 Summary and Discussion

A coupled African easterly wave-mesoscale convective system (AEW-MCS) was examined over the Arabian Peninsula and East Africa in August 2004. The AEW-MCS (denoted as A04), was identified through satellite brightness temperature and ERA-I total cloud cover. A04's convective and vorticity origins was found to be over the southern Arabian Peninsula and propagated in to East Africa. The vorticity fields analyzed from the ERA-I was then examined to trace A04's pre-AEW vorticity perturbation. From origin to the mature stage of A04, the propagation speed was 7.6 m s^{-1}. The formation of A04's pre-AEW vorticity perturbation was on 8/9/00Z located at (15°N, 47°E). A vorticity budget was then performed to investigate the formation mechanisms from the ERA-I data. It was found that planetary vorticity stretching associated with cyclonic convergence from the interaction of the Arabian high and Indian Ocean high, generates the pre-AEW vorticity perturbation associated with A04. While the analysis of the ERA-I data provides basis for significant findings for the formation mechanism using vorticity, it does not resolve well the orographic effects and mesoscale processes from the southern Arabian Mountains and Ethiopian Highlands.

To search for the origin and find the formation of A04, a numerical simulation using the WRF model was performed using the ERA-I data as the initial field. Higher resolution results provided the information needed to explain the origin of A04's pre-AEW vorticity perturbation, especially over the mountains. It was found that the higher resolution results produced a stronger zonal wind flow over East Africa and the Arabian Peninsula, which would directly increase the magnitudes of the vorticity field. There was also more vorticity generation processes resolved over the mountains, especially during diurnal cycles. The vorticity budget was performed on the numerical simulation and the results were as follows:

1) The overall vorticity budget from the numerical simulation increased in magnitude, with the vorticity advection having the highest order of 10^{-9} s^{-2}. A04's pre-AEW vorticity perturbation is highly influenced from easterly wind flow and the zonal gradient that increases vorticity intensity.
2) The convergence of planetary vorticity explains the generation of vorticity over the southern Arabian Peninsula. The Arabian high produces northeasterly wind over Arabia and the Indian Ocean high produces southwesterly wind. When these highs begin to converge, cyclonic vorticity is generated over the southern Arabian Peninsula, particularly during diurnal cycles when lee vorticities are produced from orographic effects.

A04 went through 3 phases: formation, merging, and mature. Two pre-AEW and pre-MCS systems were associated with the formation stage, which one was over the Ethiopian Highlands (PAM-1) and the other over the southern Arabian Mountains (PAM-2) at 8/9/06Z. These areas are part of the stationary mode of lee generated vorticity and convective generation from the diurnal cycle. Once generated, the systems propagate away from their respected mountain region. During the merging phase starting at 8/11/06Z, PAM-1 begins to slow down as it nears the Darfur Mountains while PAM-2 continues to propagate at a constant speed of 8.5 m s^{-1} over the Ethiopian Highlands and into Sudan. At 8/13/06Z, PAM-1 and PAM-2 have merged together over the Darfur Mountains and formed into a mature AEW-MCS system, which is known as A04 throughout this case study. The diurnal cycle and convective cloud burst over the next 12 h enhances the systems as it continues to propagate to the west.

The eastern local wind maximum (LWM_E) of the Africa easterly jet was also investigated to show how A04's PAM-2 is maintained by easterly wind flow. As PAM-2 propagates to the west, the easterly wind flow also increases under the influence of the Arabian high. The high pressure system induces a strong meridional geopotential gradient that will increase easterly wind on the southern rim of the high. Once over Sudan, the LWM_E is mature and the presence of westerly wind south of the easterly wind flow will produce a stronger zonal gradient. Over Sudan is when PAM-1 and PAM-2 began to merge. Once A04 is mature and propagate to the west of the Darfur Mountains, the LWM_E will be intercepted by the influence of the Saharan high.

This research investigated the formation of an AEW-MCS system, while neglecting potential vorticity and potential temperature analysis. Analysis performed in this study was from a mechanical perspective, which the main concern was the generation of vorticity over the southern Arabian Peninsula due to convergence. The mechanical mechanism has been established, but more work will be needed to investigate A04's effects from heating and the creation and destruction of potential vorticity. This will also provide more information on adiabatic processes that aids in the development of convection of East African and southern Arabian Peninsula.

CHAPTER 5

Conclusions

The African Easterly Jet was analyzed for the month of August between 1976 and 2010 as well as 2006 as a case study to demonstrate a second maximum core located in East Africa centered around (15^{o}N, 35^{o}E). Once this maximum was identified, there was a series of examinations that explained the dynamical interactions of the LWM_E and the East African synoptic circulations. The LWM_E is located south of the Arabian high much like the LWM_W located south of the Saharan high. The increased intensity of the LWMs associated with AEJ is due to the maximum meridional geopotential gradient from the Saharan and Arabian highs, which causes the AEJ to be mainly geostrophic. From the east-west circulation, there were two distinct divergence flows in the mid-levels that were over Africa and the Arabian Peninsula. The upward vertical motion is associated with the ITF heating in which the Saharan and the Arabian thermal lows are located. The rising of warm air converges with the sinking cooler air forming divergence centers over Africa and the Arabian Peninsula. This differential heating from the divergent centers help maintain the anticyclones. The formation and evolution of the Arabian high begins in March reaching peak intensity in May, August, and October and the LWM_E is at maximum intensity during August.

At 600 mb during August (1979-2010) there exist the Saharan and Arabian highs, African easterly jet (AEJ) with two embedded local wind maxima in West and East Africa, and easterly waves over Arabia and Africa easterly waves (AEWs) over Africa. The highest variability occurs over Central Africa, Eastern Africa, and the Arabian Peninsula. For all synoptic systems present, positive (negative) ENSO years will decrease (increase) intensity. For East Africa, the Arabian high's intensity will either increase or decrease the intensity of LWM_E. The LWM_E will help maintain the propagation of easterly waves, especially during extreme Non-ENSO years where the westerly jet reaches into the mid-troposphere and enhance easterly wave intensity. For the AEJ, the zonal gradient is weaker during ENSO years compared to that during Non-ENSO years. This zonal gradient is important in modulating the easterly wave intensity, especially over the Arabian Peninsula. When a strong zonal gradient is present over the Arabian Peninsula, it can help maintain easterly wave propagation.

A coupled African easterly wave-mesoscale convective system (AEW-MCS) was examined over the Arabian Peninsula and East Africa in August 2004. It was found that planetary vorticity stretching associated with cyclonic convergence from the interaction of the Arabian high and Indian Ocean high, generates the pre-AEW relative vorticity perturbation associated with A04. While the analysis of the ERA-I data provides basis for significant findings for the formation mechanism using vorticity, it does not resolve well the orographic effects and mesoscale processes from the southern Arabian Mountains and Ethiopian Highlands.

Higher resolution results provided the information needed to explain the origin of A04's vorticity perturbation, especially over the mountains. It was found that the higher resolution results produced a stronger zonal wind flow over East Africa and the Arabian Peninsula, which would directly increase the magnitudes of the vorticity field. There was also more vorticity generation processes resolved over the mountains, especially during diurnal cycles. The vorticity budget was performed on the numerical simulation and the results were as follows:

1) The overall vorticity budget from the numerical simulation increased in magnitude, with the vorticity advection having the highest order of 10^{-9} s^{-2}. A04's vorticity perturbation is highly influenced from easterly wind flow and the zonal gradient that increases vorticity intensity.

2) The convergence of planetary vorticity explains the generation of vorticity over the southern Arabian Peninsula. The Arabian high produces northeasterly wind over Arabia and the Indian Ocean high produces southwesterly wind. When these highs begin to converge, cyclonic vorticity is generated over the southern Arabian Peninsula, particularly during diurnal cycles when lee vorticities are produced from orographic effects.

A04 went through 3 phases: formation, merging, and mature. Two pre-AEW and pre-MCS systems were associated with the formation stage, which one was over the Ethiopian Highlands (PAM-1) and the other over the southern Arabian Mountains (PAM-2) at 9/06Z. These areas are part of the stationary mode of lee generated vorticity and convective generation from the diurnal cycle. Once generated, the systems propagate away from their respected mountain region.

The eastern local wind maximum (LWM_E) of the Africa easterly jet was also investigated to show how A04's PAM-2 is maintained by easterly wind flow. As PAM-2 propagates to the west, the easterly wind flow also increases under the influence of the Arabian high. The high pressure system induces a strong meridional geopotential gradient that will increase easterly wind on the southern rim of the high. Once over Sudan, the LWM_E is mature and the presence of westerly wind south of the easterly wind flow will produce a stronger zonal gradient. Over Sudan is when PAM-1 and PAM-2 began to merge. Once A04 is mature and propagate to the west of the Darfur Mountains, the LWM_E will be intercepted by the influence of the Saharan high.

References

Berry G. J., C. D. Thorncroft, 2005: Case study of an intense African easterly wave. *Mon Weather Rev*., **133**, 752 - 766.

Bjerknes, J., 1969: Atmospheric teleconnections from the equatorial Pacific. *Mon. Wea. Rev.*, **97**, 163–172.

Bluestein, H. B., 1992: Synoptic-Dynamic Meteorology in Midlatitudes. Vol. 1, Oxford University Press

Burpee, R. W., 1972: The origin and structure of easterly waves in the lower troposphere of North Africa. *J. Atmos. Sci.*, **29**, 77 - 90.

Burpee, R. W., 1974: Characteristics of the North African easterly waves during the summers of 1968 and 1969. *J. Atmos. Sci*., **31**, 1556 - 1570.

Carlson, T. N., 1969: Synoptic histories of three African disturbances that developed into Atlantic hurricanes. *Mon. Wea*. Rev., **97**, 256 - 276.

Chang, C. B., 1993: Impact of desert environment on the genesis of African wave disturbances. *J. Atmos. Sci*., **50**, 2137 - 2145.

Charney, J. G., and M. E. Stern, 1962: On the stability of internal baroclinic jets in a rotating atmosphere. *J. Atmos. Sci*., **19**, 159 - 172.

Chen, T.-C., 2005: Maintenance of the midtropospheric North African summer circulation: Saharan high and African easterly jet. *J. Climate*., **18**, 2943 - 2962.

Chen, T.-C., 2006: Characteristics of African easterly waves depicted by ECMWF Reanalysis for 1991-2000. *Mon. Wea. Rev*., **134**, 3539 - 3566.

Cook, K. H., 1999: Generation of the African Easterly Jet and Its Role in Determining West African Precipitation. *J. Climate*, **12**, 1165 - 1184.

Cornforth, R. J., B. J. Hoskins, C. D. Thorncroft, 2009: Impact of moist processes on the African Easterly Jet-African Easterly Waves system. *Ouart. J. Roy. Meteor. Soc*., **135**, 894-913.

Dee, D. P. et al., 2011: The ERA-Interim reanalysis: configuration and performance of the data assimilation system. *Quart. J. Roy. Meteor. Soc*., **137**, 553 - 597.

Dezfuli, A. K., and S. E. Nicholson, 2010: A note on long term variations of the African easterly jet. *Int. J. Climatol.*, **31**, 2049 - 2054. doi: 10.1002/joc.2209.

Dudhia, J., 1989: Numerical study of convection observed during the winter monsoon experiment using a mesoscale two-dimensional model, J. Atmos. Sci., **46**, 3077–3107.

Fink, A. H., and A. Reiner, 2003: Spatio-temporal variability of the relation between African easterly waves and West African squall lines in 1998 and 1999. *J. Geophys. Rev*., **108**, 4332.

Gaetani, M., M. Baldi, G. A. Dalu, and G. Maracchi. 2011: Jetstream and rainfall distribution in the Mediterranean region. *Nat. Hazards Earth Syst. Sci*., **11**, 1-14. doi:10.5194/nhess-11-1-2011

Glickman, T. S. (ed.), 2000: *Glossary of Meteorology*. 2nd Ed., Amer. Meteor. Soc., 855pp.

Grist, J. P., S. E. Nicholson, and A. L. Barcilon, 2002: Easterly wave over Africa. Part II: Observed and modeled contrast between wet and dry years. *Mon. Wea. Rev*., **130**, 212 - 225.

Hodges, K. I., and C. D. Thorncroft, 1997: Distribution and statistics of African mesoscale convective weather systems based on ISCCP Meteosat imagery. *Mon. Wea. Rev*., **125**, 2821 - 2837

Holton, J. R., 2004: *An Introduction to Dynamic Meteorology*.4th Edition, Elsevier Academic Press.

Hsieh, J.-S., and K. H. Cook, 2005: Generation of African easterly wave disturbances: Relationship to the African easterly jet. *Mon. Wea. Rev*., **133**, 1311 - 1327.

Hsieh, J.-S., and K. H. Cook, 2007: A study of the energetics of African easterly waves using a regional climate model. *J. Atmos. Sci*., **64**, 2212 - 2230.

Hulme, M., 2001. Climate perspectives on Sahelian dessiccation: 1973–1998. *Global Environ. Change* **11**: 19–29.

Hurlburt, H. E., J. Dana Thompson, 1976: A Numerical Model of the Somali Current. *J. Phys. Oceanogr.*, **6**, 646 - 664.

Janjic, Z. I., 1994: The step-mountain eta coordinate model: further developments of the convection, viscous sublayer and turbulence closure schemes, Mon. Wea. Rev., **122**, 927–945.

Kalnay, E., and Coauthors, 1996: The NCEP/NCAR 40-Year Reanalysis Project. *Bull. Amer. Meteor. Soc.*, **77**, 437 - 471.

Knapp, K. R., S. Ansari, C. L. Bain, M. A. Bourassa, M. J. Dickinson, C. Funk, C. N. Helms, C. C. Hennon, C. D. Holmes, G. J. Huffman, J. P. Kossin, H.-T. Lee, A. Loew, and G.Magnusdottir, 2011: Globally gridded satellite (GridSat) observations for climate studies. *Bull. Amer. Meteor. Soc.*, **92**, 893–907.

Kruger, A. C., and S. Shongwe, 2004: Temperature trends in South Africa: 1960-2003. *Int. J. Climatol*., **24**, 1929–1945.

Kwon, H. J., 1989: A re-examination of the genesis of African waves. *J. Atmos. Sci*., **46**, 3621 – 3631.

Laing, A. G., and J. M. Fritsch, 1993: Mesoscale convective complexes in Africa. *Mon. Wea. Rev*., **121**, 2254 - 2263.

Landsea, C. W., 1993: A climatology of intense (or major) Atlantic hurricanes. *Mon. Wea. Rev.*, **121**, 1703 - 1713.

Lavaysse, C., C. Flamant, S. Janicot, and P. Knippertz, 2010: Links between African easterly waves, midlatitude circulation and intraseasonal pulsations of the West African heat low. *Quart. J. Roy. Meteor. Soc*, **136**: 141 - 158. doi: 10.1002/qj.555

Lavaysse C., C. Flamant, S. Janicot, D.J. Parker, J.-P. Lafore, B. Sultan and J. Peloni, 2009, Seasonal evolution of the West African Heat Low: A Climatological perspective. *Climate Dynamics*, DOI : 10.1007/s00382-009-0553-4

Lin, Y.-L., 2007: *Mesoscale Dynamics.* Cambridge University Press, 630pp.

Lin, Y.-L., L. Liu, G. Tang, J. Spinks, and W. Jones, 2013: Origin of the pre-Tropical Strom Debby (2006) African easterly wave-mesoscale convective system. *Meteor.Atmos. Phys.*, **120**, 123 – 144.

Lin, Y.-L, K. E. Robertson, and C. M. Hill, 2005: Origin and propagation of a disturbance associated with an African easterly wave as a precursor of Hurricane Alberto (2000). *Mon. Wea. Rev.*, **133**, 3276 - 3298.

Mass, C., 1979: A linear primitive equation model of African wave disturbances. *J. Atmos. Sci*. **36**, 2075 - 2092.

Mekonnen, A., C. D. Thorncroft, and A. R. Aiyyer, 2006: Analysis of convection and its association with African easterly waves. *J. Climate*, **19**, 5405 - 5421.

Mlawer, E. J., S. J. Taubman, P. D. Brown, M. J. Iacono, and S. A. Clough, 1997: Radiative transfer for inhomogeneous atmosphere: RRTM, a validated correlated k model for the longwave. J. Geophys. Res., **102** (D14), 16663–16682.

Mozer, J. B., and J. A. Zehnder, 1995: Lee vorticity production by large-scale tropical mountain ranges. part ii: a mechanism for the production of African waves. *J. Atmos. Sci.*, **53**, 539 - 549.

Parker, D. J., C. D. Thorncroft, R.R. Burton, A. Diongue-Niang, 2005: Analysis of the African easterly jet using aircraft observations from the JET2000 experiment. *Quart. J. Roy. Meteor. Soc*, **131**(608): 1461 - 1482.

Payne, S. W., and M. M. McGarry, 1977: The relationship of satellite inferred convective activity to easterly waves over West Africa and the adjacent ocean during phase III of GATE. *Mon. Wea. Rev.*, **105**, 413 - 420.

Philander, S.G.H., 1990: El Niño, La Niña, and the Southern Oscillation, Academic Press.

Pielke, Jr., R. A., and C. W. Landsea, 1998: Normalized hurricane damages in the United States: 1925-95. *Weather Forecasting*, **13**, 621 - 631.

Rao, P. G., H. R. Hatwar, H. H. Al-Sulaiti, and A. H. Al-Mulia, 2003: Summer Shamals over the Arabian Gulf. *Weather*, **58**, 472 - 478.

Reed, R. J., D. C. Norquist, and E. E. Recker, 1977: The structure and properties of African wave disturbances as observed during Phase III of GATE. *Mon. Wea. Rev.*, **105**, 317 - 333.

Rennick, M. A., 1976: The generation of African waves. *J. Atmos. Sci.*, **33**,1955 - 1969.

Saha, S. et al., 2006: The NCEP Climate Forecast System. *J. Climate*, **19**, 3483 - 3517.

Sathiyamoorthy, V., P. K. Pal, and P.C. Joshi, 2006: Intraseasonal variability of the Tropical Easterly Jet. *Meteorology and Atmospheric Physics*, **96**, 305-316.

Semazzi, F. H. M., and M. Indeje., 1999. Inter-seasonal variability of ENSO rainfall signal over Africa. *Journal of the African Meteorological Society*, **4**, 81 – 94.

Simmons, A. J., 1977: A note on the instability of the African easterly jet. *J. Atmos. Sci*., **34**, 1670 - 1674.

Skamarock, W. C., J. B. Klemp, J. Dudhia, D. O. Gill,D. M. Barker, W. Wang, and J. G. Powers, 2008:Adescription of the Advanced Research WRF version 3. NCAR technical note.TN-4751STR, 113 pp. http://www.mmm.ucar.edu/wrf/users/docs/arw_v3.pdf

Tao, W.-K., J. Simpson, and M. McCumber 1989: An ice-water saturation adjustment, Mon. Wea. Rev.,117, 231–235.

Thorncroft, C. D., 1995: An idealized study of African easterly waves. Part III: more realistic basic states. *Quart. J. Roy. Meteor. Soc*., **121**, 1589 - 1614.

Thorncroft, C. D., N. M. Hall, G. N. Kiladis, 2008: Three-dimensional structure and dynamics of African easterly waves. Part III: genesis. *J. Atmos. Sci.,* **65**, 3596 - 3607.

Thorncroft, C. D., and B. J. Hoskins, 1994a: An idealized study of African easterly waves. Part I: a linear view. *Quart. J. Roy. Meteor. Soc*., **120**, 953 - 982.

Thorncroft, C. D., and B. J. Hoskins, 1994b: An idealized study of African easterly waves. Part II: a nonlinear view. *Quart. J. Roy. Meteor. Soc*., **120,** 983 - 1015.

Thorncroft, C. D., D. J. Parker, R. R. Burton, M. Diop, J. H. Ayers, H. Barjat, S. Devereau, A. Diongue, R. Dumelow, D. R. Kindred, N. M. Price, M. Saloum, C. M. Tayor, and A.M. Tompkins: The Jet2000 Project: Aircraft observations of the African easterly jet and African easterly waves. *Bull. Amer. Meteor. Soc*., **84**, 337 - 351.

Uppala, S.M. et al., 2005: The ERA-40 re-analysis. *Quart. J. R. Meteorol. Soc*., **131**, 2961-3012.doi:10.1256/qj.04.176

Wolter, K., 1987: The Southern Oscillation in surface circulation and climate over the tropical Atlantic, Eastern Pacific, and Indian Oceans as captured by cluster analysis. *J. Climate Appl. Meteor.*, **26**, 540-558.

Wolter, K., and M.S. Timlin, 1993: Monitoring ENSO in COADS with a seasonally adjusted principal component index. *Proc. of the 17th Climate Diagnostics Workshop,* Norman, OK, NOAA/NMC/CAC, NSSL, Oklahoma Clim. Survey, CIMMS and the School of Meteor., Univ. of Oklahoma, 52-57.

Wolter, K., and M. S. Timlin, 1998: Measuring the strength of ENSO events - how does 1997/98 rank? *Weather,* **53,** 315-324.

Wolter, K., and M. S. Timlin, 2011: El Niño/Southern Oscillation behaviour since 1871 as diagnosed in an extended multivariate ENSO index (MEI.ext). *Intl. J. Climatology*, **31**, 1074 - 1087.

Wu, M.-L. C., O. Reale, S.D. Schubert, M.J. Suarez, R.D. Koster, P.J. Pegion, 2009: African easterly jet: Structure and maintenance. *J. Climate*, **22**, 4459 - 4480.